Event shape engineering for inclusive spectra and elliptic flow in Pb-Pb collisions at √sNN=2.76 TeV

(ALICE Collaboration) Adam, J.; ...; Antičić, Tome; ...; Erhardt, Filip; ...; Gotovac, Sven; ...; Mudnić, Eugen; ...; ...

Event-shape engineering for inclusive spectra and elliptic flow in Pb-Pb collisions at $\sqrt{s_{NN}} = 2.76$ TeV

J. Adam *et al.*[*]

(ALICE Collaboration)

We report on results obtained with the event-shape engineering technique applied to Pb-Pb collisions at $\sqrt{s_{NN}} = 2.76$ TeV. By selecting events in the same centrality interval, but with very different average flow, different initial-state conditions can be studied. We find the effect of the event-shape selection on the elliptic flow coefficient v_2 to be almost independent of transverse momentum p_T, which is as expected if this effect is attributable to fluctuations in the initial geometry of the system. Charged-hadron, -pion, -kaon, and -proton transverse momentum distributions are found to be harder in events with higher-than-average elliptic flow, indicating an interplay between radial and elliptic flow.

I. INTRODUCTION

Results from lattice quantum chromodynamics [1,2] predict the existence of a plasma of deconfined quarks and gluons, known as the "quark gluon plasma" (QGP). This state of matter can be produced in the laboratory by colliding heavy nuclei at relativistic energies [3–5]. The QGP was found to behave as a nearly perfect liquid and its properties can be described using relativistic hydrodynamics (for a recent review, see Ref. [6]). The current experimental heavy-ion programs at Brookhaven's Relativistic Heavy Ion Collider and at CERN's Large Hadron Collider (LHC) are aimed at a precise characterization of the QGP, in particular of its transport properties.

The system created in a heavy-ion collision expands and hence cools down, ultimately undergoing a phase transition to a hadron gas, which then decouples to the free-streaming particles detected in the experiments [6]. A precision study of the QGP properties requires a detailed understanding of this expansion process. If the initial geometry of the interaction region is not azimuthally symmetric, a hydrodynamic evolution of a nearly ideal liquid (i.e., with a small value of the shear viscosity over entropy ratio η/s) gives rise to an azimuthally anisotropic distribution in momentum space for the produced particles. This anisotropy can be characterized in terms of the Fourier coefficients v_n of the particle azimuthal distribution [7]. The shape of the azimuthal distribution, and hence the values of these Fourier coefficients, depend on the initial conditions and on the expansion dynamics. The geometry of the initial state fluctuates event by event and measurements of the resulting v_n fluctuations pose stringent constraints on initial-state models. A quantitative understanding of the initial geometry of the produced system is therefore of primary importance [6]. A number of different experimental measurements and techniques have been proposed to

disentangle the effects of the initial conditions from QGP transport, including measurements of correlations of different harmonics [8], event-by-event flow fluctuations [9–12], and studies in ultracentral collisions [13,14]. Recent results from pp and p-Pb collisions at the LHC, moreover, suggest that hydrodynamic models may be also applicable to small systems [15–19]. This further highlights the importance of studying Pb-Pb collisions with more differential probes, to investigate the interplay between the initial conditions and the evolution, in the system where the hydrodynamic models are expected to be most applicable.

One of the new tools for the study of the dynamics of heavy-ion collisions is the "event shape engineering" (ESE) [20]. This technique is based on the observation that the event-by-event variation of the anisotropic flow coefficient (v_n) at fixed centrality is very large [12]. Hydrodynamic calculations show that the response of the system to the initial spatial anisotropy is essentially linear for the second and third harmonic, meaning that the final state v_2 (and v_3) are very well correlated with the second (and third) order eccentricities in the initial state for small values of η/s [7,21,22]. These observations suggest a possibility to select events in heavy-ion collisions based on the initial (geometrical) shape, providing new opportunities to study the dynamics of the system evolution and the role of the initial conditions.

The ESE technique is proposed to study ensemble-averaged observables (such as v_2 and inclusive particle spectra) in a class of events corresponding to the same collision centrality, but different v_n values. In this paper events are selected based on the magnitude of the second-order reduced flow vector q_2 (see Sec. III A). The technique was recently applied to study correlations between different flow harmonics in the ATLAS experiment [23]. In this paper we present the results on elliptic flow and charged-particle spectra in Pb-Pb collisions at $\sqrt{s_{NN}} = 2.76$ TeV obtained with the ESE technique. The events selected with the ESE technique are characterized by the measurement of v_2 to quantify the effect of the selection on the global properties of the event. To search for a connection between elliptic and radial flow the effect of the ESE selection on the inclusive transverse momentum distribution of charged hadrons, pions, kaons, and protons is then studied. The

---

[*]Full author list given at the end of the article.

results are presented for primary charged particles, defined as all prompt particles produced in the collision including all decay products, except those from weak decays of light flavor hadrons and of muons. The differential measurement described in this work could provide important constraints to identify the correct model for initial conditions and for the determination of transport properties. The development of flow in hydrodynamical models is driven by the pressure gradients and anisotropy in the initial state. A correlation between anisotropic and radial flow may stem from the specific fluctuation pattern in the initial state and/or can be produced in the final state depending on the bulk and shear viscosity of the system [7].

A few important caveats, which can affect the selectivity of the ESE technique, have to be kept in mind in this study. First, the discriminating power of the q_2 selection depends on the multiplicity and v_2 value in the pseudorapidity, η, region where it is computed and on the intrinsic resolution of the detector used for the measurement. Second, nonflow effects (such as resonance decays, jets, etc. [22]) could bias the q_2 measurement. In this work we discuss both aspects in detail, making use of different detectors with different intrinsic resolution and different η coverage.

The paper is organized as follows. In Sec. II a brief review of the ALICE detector and of the data sample is presented. In Sec. III the analysis technique, with an emphasis on the event selection and the particle identification strategy, is discussed. The results are presented in Sec. IV. Their implication for the hydrodynamic interpretation is discussed in Sec. V. Finally, we come to our conclusions in Sec. VI.

II. ALICE DETECTOR AND DATA SAMPLE

The ALICE detector at the CERN LHC was designed to study mainly high-energy Pb-Pb collisions. It is composed of a central barrel ($|\eta| \lesssim 0.8$ for full-length tracks), containing the main tracking and particle identification detectors, complemented by forward detectors for specific purposes (trigger, multiplicity measurement, centrality determination, muon tracking). A detailed description of the apparatus can be found in Ref. [24]. The main detectors used for the analysis presented in this paper are discussed below.

The main tracking devices in the central barrel are the inner tracking system (ITS) and the time projection chamber (TPC). They are immersed in a 0.5-T solenoidal field. The ITS is the detector closest to the interaction point. It is a six-layer silicon tracker with a very low material budget ($\sim 7\%$ of one radiation length X_0). The ITS provides information on the primary interaction vertex and is used to track particles close to the interaction point, with the first layer positioned at a radial distance of 3.9 cm from the interaction point and the sixth one at 43 cm. It can measure the transverse impact parameter (DCA$_{xy}$) of tracks with a resolution of about 300 (40) μm, for transverse momentum $p_T = 0.1$ (4) GeV/c, allowing the contamination from secondary particles to be significantly reduced. The TPC [25] is a large-volume gas detector (external diameter 5 m) which measures up to 159 space points per track, providing excellent tracking performance and momentum resolution ($\sigma_{p_T}/p_T \sim 6\%$ at $p_T = 10$ GeV/c) [26]. It is also

used in this work to identify particles through the measurement of the specific energy loss, dE/dx. The dE/dx, computed as a truncated mean utilizing only 60% of the available samples, has a resolution of $\sim 5\%$ in peripheral and $\sim 6.5\%$ in central collisions [26]. At a radius of 3.7 m from the beam axis, the time-of-flight (TOF) detector measures the arrival time of particles with a total resolution of about 85 ps in Pb-Pb collisions, allowing a π/K (K/p) 2σ separation up to $p_T = 3(5)$ GeV/c. The ALICE reconstruction software performs tracking based either on the information from the TPC alone (TPC-only tracks) or on the combined information from the ITS and TPC (global tracks). The former have the advantage of an essentially flat azimuthal acceptance and are used for v_2 and q_2 measurements. The latter provide better quality tracks ($\sigma_{p_T}/p_T \sim 1.5\%$ at $p_T = 10$ GeV/c) [26], rejecting most of the secondary tracks. However, the acceptance and reconstruction efficiency of global tracks are not flat in azimuth and as a function of transverse momentum, mostly owing to missing or inefficient regions of the ITS. These tracks are used for the p_T distribution measurements. TPC-only tracks can be constrained to the primary vertex (reconstructed also using the ITS information) to provide better momentum resolution.

The data used for this analysis were collected in 2010, during the first Pb-Pb run at the LHC, at a center-of-mass energy per nucleon $\sqrt{s_{NN}} = 2.76$ TeV. The hadronic interaction rate was of the order of 100 Hz, low enough to avoid any space charge distortion effects in the TPC [27]. The trigger was provided by the V0 detector [28], a pair of forward scintillator hodoscopes placed on either side of the interaction region, covering the pseudorapidity regions $2.8 < \eta < 5.1$ (V0A) and $-3.7 < \eta < -1.7$ (V0C). Events were requested to have a signal in both sides of the V0, selecting roughly 0%–90% most central collisions [29]. The V0 measures a signal whose average amplitude is proportional to the multiplicity of charged particles. The V0 acceptance times detection efficiency is approximately 90% and flat as a function of the particle p_T, with only a small reduction to about 85% for $p_T < 300$ MeV/c. Events are further selected offline using the timing information from the V0 and from a set of two forward zero-degree calorimeters (ZDCs), to reject contamination from beam-induced backgrounds (see Refs. [29–31] for a detailed discussion). After all selections, the event sample used in the analysis consists of about 16×10^6 events.

III. ANALYSIS TECHNIQUE

A. Centrality and the event-shape selection

The events which pass the basic selection described in Sec. II are divided in centrality classes based on the signal amplitude (proportional to the charged-particle multiplicity) measured in the V0 detector, as described in Ref. [29]. Events in each centrality class are further subdivided into groups with different average elliptic event shapes based on the magnitude of the second-order reduced flow vector q_2 [22] given as

$$q_2 = \frac{|\boldsymbol{Q}_2|}{\sqrt{M}}, \tag{1}$$

where M is the multiplicity and $|\boldsymbol{Q}_2| = \sqrt{Q_{2,x}^2 + Q_{2,y}^2}$ is the magnitude of the second-order flow vector.

In this paper, the flow vector $\boldsymbol{Q}_2$ is calculated using the TPC or V0 detectors. In the TPC, tracks in the range $0.2 < p_T < 20$ GeV/c and $|\eta| < 0.4$ (to avoid an overlap with the η region used for the v_2 and p_T distribution measurements) are used to measure

$$Q_{2,x} = \sum_{i=1}^{M} \cos 2\varphi_i, \quad Q_{2,y} = \sum_{i=1}^{M} \sin 2\varphi_i, \quad (2)$$

where φ_i is the azimuthal angle of the ith particle and M is the number of tracks in an event.

In the forward rapidity region the V0 is used. This detector is segmented into four rings, each consisting of eight azimuthal sectors; the flow vector is hence calculated as

$$Q_{2,x} = \sum_{i=1}^{32} w_i \cos 2\varphi_i,$$

$$Q_{2,y} = \sum_{i=1}^{32} w_i \sin 2\varphi_i, \quad M = \sum_{i=1}^{32} w_i, \quad (3)$$

where the sum runs over all 32 channels, φ_i is the angle of the center of the sector containing channel i, w_i is the amplitude measured in channel i, and M is in this case the sum of the amplitudes measured in each channel.

The discriminating power of q_2 depends on the magnitude of elliptic flow as well as on the track multiplicity used in the q_2 calculation and on the performance of the detector, including the angular resolution or the linearity of the response to the charged particle multiplicity. The good resolution of the TPC and the large multiplicity at midrapidity are used to maximize the selectivity on q_2. However, the ALICE central barrel acceptance enables only limited separation in pseudorapidity between the region used to calculate q_2 and the region used to calculate the observables ($|\Delta\eta| = 0.1$). This separation is introduced to suppress unwanted nonflow correlations, which typically involve only a few particles and are, in general, of short range. To further assess the contribution of nonflow correlations, the flow vector is also calculated using the V0 detectors. This leads to a separation of more than one unit in pseudorapidity between the two regions.

In the absence of correlations, the average length of $\boldsymbol{Q}_2$ grows as $\sqrt{M}$ [22]: q_2 is introduced to remove this trivial part of the multiplicity dependence. In case of nonzero correlations (owing to either collective flow or nonflow correlations), q_2 depends on multiplicity and on the strength of the flow as [22,32]

$$\langle q_2^2 \rangle \simeq 1 + \langle (M - 1)\rangle \langle (v_2^2 + \delta_2)\rangle, \quad (4)$$

where the parameter δ_2 accounts for nonflow correlations and the angular brackets denote the average over all events.

In the case when the multiplicity is measured via the signal amplitude in the V0 detector, the first term in Eq. (4) (unity) has to be substituted by $\langle e_i^2 \rangle / \langle e_i \rangle^2$, where e_i is the energy deposition of a single particle i. The fluctuations in e_i lead to an increase in the flow vector length and reduce the corresponding event plane resolution.

The q_2 distribution measured with the TPC (q_2^{TPC}) and V0C (q_2^{V0C}) is shown in Fig. 1 as a function of centrality and in two narrow centrality classes, 0%–1% and 30%–31%. As can be seen, q_2 reaches values twice as large as the mean value, as expected in case of large initial-state fluctuations [20]. The q_2^{V0C} is larger than q_2^{TPC}, as the former is measured in a larger pseudorapidity window (integrating a larger multiplicity) and is sensitive to the fluctuations in e_i. Note also that the selectivity (discrimination power) of the two selection cuts is, in principle, different, owing to the different detector resolution, and, in the case of V0C, smaller v_2 value at forward η, fluctuations in e_i, and large contribution of secondary particles.

In the present analysis, the effect of the ESE on v_2 and p_T distributions is studied. The average flow and particle spectra are measured in the pseudorapidity range $0.5 < |\eta| < 0.8$ to avoid overlap with the region used to calculate q_2^{TPC}. The V0C selection is used to estimate the contribution of nonflow correlations to the event-shape selection, because it provides a large η gap. As a further cross-check, the analysis was also repeated using the V0A detector. The results obtained with V0A and V0C show a qualitative agreement with a better selectivity when the V0C is used (mostly owing to the larger multiplicity in the acceptance of this detector and to the η dependence of the elliptic flow). We therefore report the results for events selected using q_2^{TPC} and q_2^{V0C} in this paper.

Owing to the limited statistics, the analysis has to be performed in relatively wide centrality classes ($\sim$10%). The length of q_2 changes within such large centrality intervals (Fig. 1), and a cut at a fixed value of q_2 would introduce a dependence on the multiplicity that would obscure the effect of the event-shape selection. The q_2 selection is therefore evaluated in narrow (1%-wide) centrality classes. The results presented in the next sections are obtained in two event-shape classes, corresponding to the 10% of the events having the top (bottom) value of the q_2 (estimated in the narrow centrality classes). In the following, we refer to these two classes as "large-q_2" (90%–100%) and "small-q_2" (0%–10%) or, generically, as ESE-selected events. Conversely, we refer to the totality of data within a given centrality class as the "unbiased" sample.

The correlation between q_2^{TPC} and q_2^{V0C} is illustrated for events in the 30%–31% centrality class in Fig. 2. The left (right) panel shows the distribution of q_2 measured with the TPC (V0C) for all events and for events in the large-q_2 and small-q_2 classes, selected with the V0C (TPC). The average q_2 changes by about 18% and 14% in the large-q_2 and small-q_2 samples, respectively. To control the effect of fluctuations in a given detector, the detailed comparison of the results obtained with q_2^{TPC} and q_2^{V0C} is crucial, as discussed in detail below. To disentangle the effect of the η gap and of the q_2 cut, the selection on q_2^{TPC} is also adjusted such that the average flow measured at midrapidity is similar to the one in the large-q_2 sample (Sec. IV).

The ESE becomes less selective in peripheral events regardless of the detector used to compute q_2, owing to the low multiplicity. This limits the present analysis to the 60% most central events.
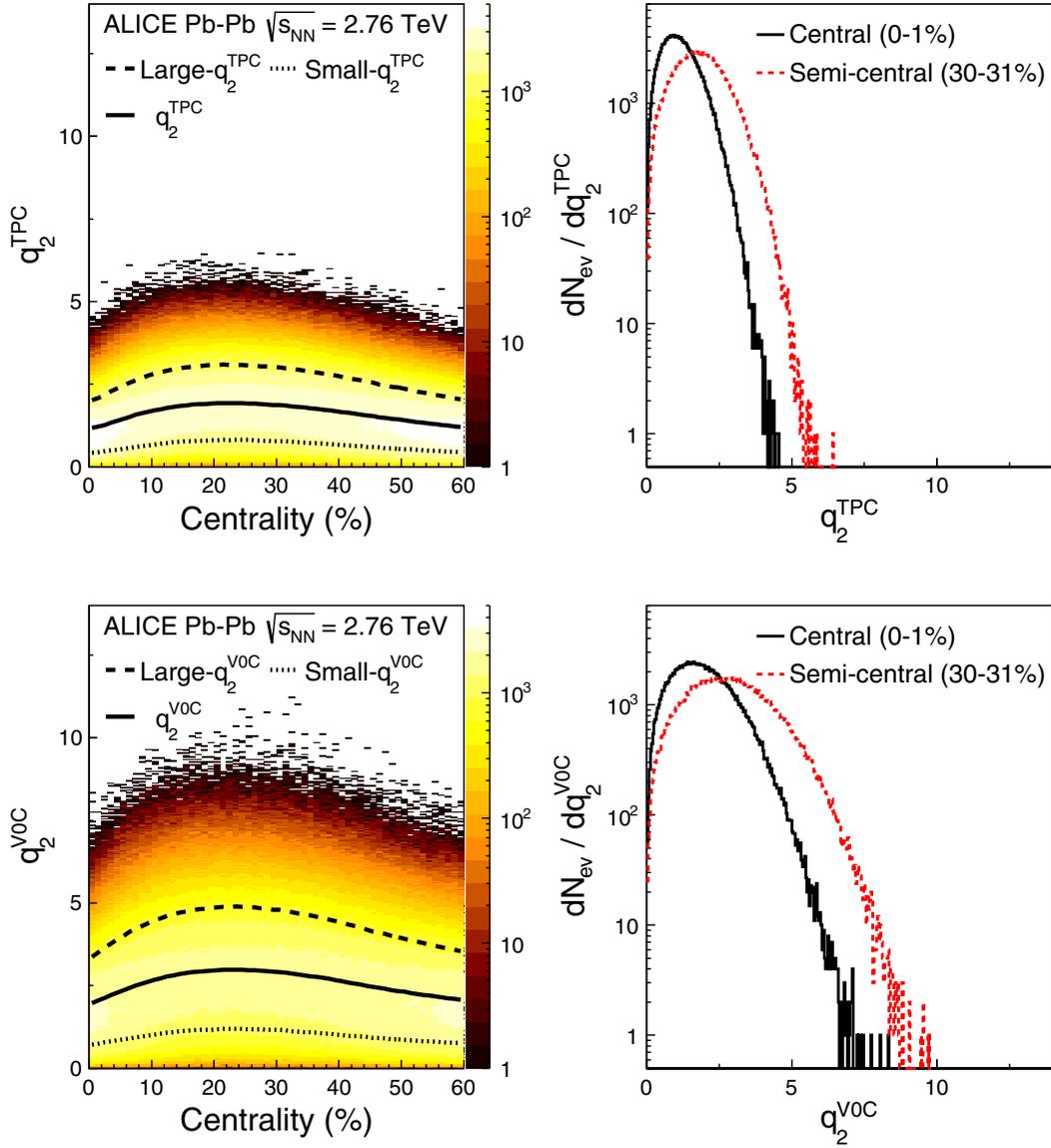
FIG. 1. Distributions of q_2^{TPC} (top row) and q_2^{V0C} (bottom row) as a function of centrality (left column) and projections for two centrality classes, 0%–1% and 30%–31% (right column). In each of the left panels the solid curve shows the average q_2 as a function of centrality, while the dashed and the dotted curves indicate the top 10% and the bottom 10%, respectively.

Space charge distortion effects in the TPC, which accumulate over many events, could, in principle, bias the q_2 selection. To check for this and other possible instrumental effects, it was verified that the results are not sensitive to the instantaneous luminosity.

B. Elliptic flow measurement

The elliptic flow, v_2, is measured in the pseudorapidity range $0.5 < |\eta| < 0.8$ using the scalar-product (SP) method [22], according to

$$v_2\{SP\} = \frac{\langle \boldsymbol{u}_{2,k} \boldsymbol{Q}_2^*/M \rangle}{\sqrt{\boldsymbol{Q}_2^A \boldsymbol{Q}_2^{B*}/M^A M^B}}, \quad (5)$$

where $\boldsymbol{u}_{2,k} = \exp(i2\varphi_k)$ is the particle's unit flow vector, φ_k is the azimuthal angle of the kth particle of interest, $\boldsymbol{Q}_2$ is

the flow vector, and M is the multiplicity. The full event is divided in two independent subevents, labeled A and B, covering two different pseudorapidity ranges, $0.5 < \eta < 0.8$ and $-0.8 < \eta < -0.5$. The particle's unit flow vector $\boldsymbol{u}_{2,k}$ is evaluated in the subevent A, while the flow vector $\boldsymbol{Q}_2$ and the multiplicity M in the subevent B and vice versa, ensuring a pseudorapidity gap of $|\Delta\eta| > 1$ between the particle of interest and the reference charged particles, which suppresses the nonflow contribution in the calculation of $v_2\{SP\}$. A flat acceptance in azimuth is achieved in this analysis selecting TPC-only tracks, constrained to the primary vertex. Tracks are required to have at least 70 clusters and a $\langle \chi^2 \rangle \leqslant 4$ per TPC cluster (two degrees of freedom). Tracks with a transverse distance of closest approach to the vertex (computed before constraining tracks to the primary vertex) $\text{DCA}_{xy} > 2.4$ cm or a longitudinal distance of closest approach $\text{DCA}_z > 3.2$ cm
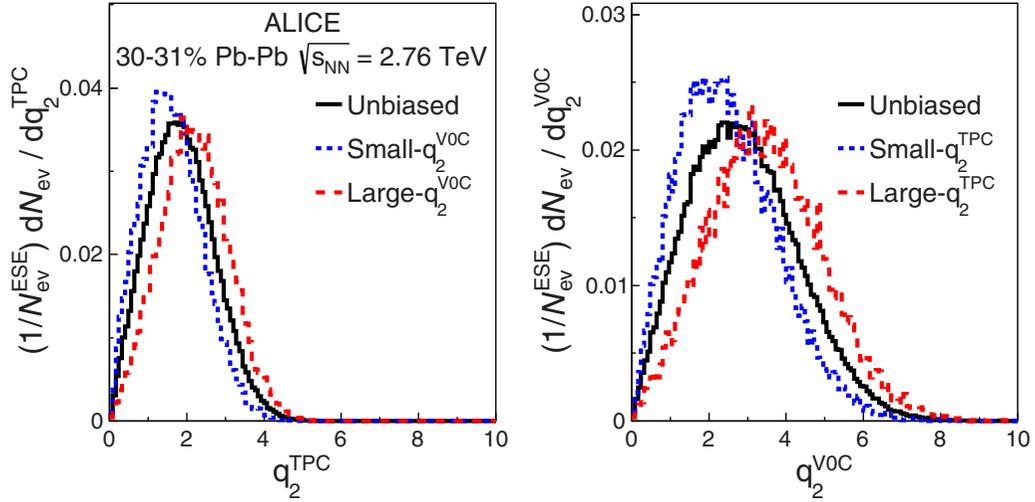
FIG. 2. Effect of the q_2^{V0C} (q_2^{TPC}) event-shape selection on the q_2^{TPC} (q_2^{V0C}) distributions for events in the 30%–31% centrality class.

are rejected to reduce the contamination from secondary tracks. The effect of secondary particles is corrected applying the same analysis procedure to Monte Carlo events, simulated with the AMPT event generator [33] and propagated through a GEANT3 [34] model of the detector. The $v_2\{SP\}$ computed using reconstructed tracks is then compared with the one computed with generated primary particles, and the difference (<5%) is used as a correction factor.

The uncertainty on the tracking efficiency was assessed with different track samples and selections: using a set of hybrid tracks, built from a combination of global and TPC-only tracks to obtain a uniform azimuthal acceptance [35], using TPC-only tracks not constrained to the primary vertex, varying the minimum number of TPC clusters required in the analysis from 70 to 50 (*track reconstruction* in Tables I and II), and weighting each track by the inverse of the (p_T-dependent) efficiency (*tracking efficiency*).

The procedure used to estimate the centrality percentiles leads to a ∼1% uncertainty in the definition of the centrality classes [29]. To propagate this uncertainty to the results presented in this paper, the measurement is repeated displacing the centrality percentile by 1%. For instance, the analysis in the 30%–40% centrality class is repeated for the selection 30.3%–40.4% (*centrality resolution*). Moreover, tracks reconstructed at midrapidity (instead of the V0 signal) are used as the centrality estimator (*centrality estimator*).

The correction for the effect of secondary particles mentioned above is strongly model dependent; therefore, the difference between the v_2 estimated using generated AMPT particles and reconstructed tracks was used to estimate the corresponding systematic uncertainty, ∼3.5% (0.7%) at $p_T =$ 0.2 (1.5) GeV/c (*secondary particles*).

Moreover, the following systematic checks were considered. The dependence on the magnetic-field configuration

TABLE I. Summary of systematic errors on $v_2\{SP\}$ measurement. NS, not statistically significant.

Effect	v_2	v_2 large-q_2	v_2 small-q_2
Track reconstruction	3.1% (0%–20%)	3.1% (0%–20%)	3.1% (0%–20%)
	2.7% (20%–60%)	2.7% (20%–60%)	2.7% (20%–60%)
	($p_T = 0.2$ GeV/c)	($p_T = 0.2$ GeV/c)	($p_T = 0.2$ GeV/c)
	0.08% (0%–20%)	0.08% (0%–20%)	0.08% (0%–20%)
	0.02% (20%–60%)	0.02% (20%–60%)	0.02% (20%–60%)
	($p_T = 1.5$ GeV/c)	($p_T = 1.5$ GeV/c)	($p_T = 1.5$ GeV/c)
Tracking efficiency	0.07%	0.35%	0.14%
Centrality resolution	0.21%	0.35%	0.35%
Centrality estimator	0.57%	0.49%	0.57%
Secondary particles	3.56%	3.56%	3.56%
	($p_T = 0.2$ GeV/c)	($p_T = 0.2$ GeV/c)	($p_T = 0.2$ GeV/c)
	0.8%	0.8%	0.8%
	($p_T = 1.5$ GeV/c)	($p_T = 1.5$ GeV/c)	($p_T = 1.5$ GeV/c)
Magnetic field	NS	NS	NS
Charge	NS	NS	NS
Vertex	NS	NS	NS

TABLE II. Summary of systematic errors on the $v_2\{SP\}$ ratios. NS, not statistically significant.

Effect	v_2 large-q_2/unbiased	v_2 small-q_2/unbiased
Track reconstruction	0.14%	0.14%
Tracking efficiency	0.35%	0.21%
Centrality resolution	0.14%	0.21%
Centrality estimator	0.14%	0.07%
Secondary particles	0.07%	0.35%
Magnetic field	NS	NS
Charge	NS	NS
Vertex	NS	NS

was studied analyzing separately samples of events collected with different polarities of the magnetic field (*magnetic field*), analyzing positive and negative particles separately (*charge*), and analyzing samples of tracks produced at different vertex positions: $-10 < z_{\text{vtx}} < 0$ cm and $0 < z_{\text{vtx}} < 10$ cm (*vertex*). These effects are found to be not significant.

The systematic uncertainties in the v_2 measurements and in the ratios of v_2 in ESE-selected over unbiased events are summarized in Tables I and II. Only the checks and variations that are found to be statistically significant are considered in the systematic uncertainties [36]. Whenever the p_T dependence of the uncertainty is not negligible, values for characteristic p_T are given in the tables.

C. Transverse momentum distribution measurement

The measurement of the p_T distributions uses global tracks, which provide good resolution on DCA$_{xy}$ (Sec. II) and hence good separation of primary and secondary particles. The track selection requires at least 70 clusters in the TPC and at least 2 points in the ITS, of which at least one must be in the first two layers to improve the DCA$_{xy}$ resolution. A p_T-dependent cut on the DCA$_{xy}$, corresponding to 7 times the experimental resolution on DCA$_{xy}$, is applied to reduce the contamination from secondary particles. Tracks with a χ^2 per point larger than 36 in the ITS and larger than 4 in the TPC are rejected. Finally, to further reduce the contamination from fake tracks, a consistency cut between the track parameters of TPC and global tracks was applied. For each reconstructed TPC track, the χ^2 difference between the track parameters computed using only the TPC information constrained to the vertex and the associated global track is required to be less than 36 [37]. Charged tracks are studied in the pseudorapidity window $0.5 < |\eta| < 0.8$, to avoid an overlap with the q_2^{TPC} calculation.

Particles are identified using the specific energy loss dE/dx in the TPC and their arrival time in the TOF. The technique is similar to the one presented in Ref. [15]. A track is identified as either a pion, a kaon, or a proton based on the difference, in the detector resolution units, from the expected energy loss and/or TOF $n\sigma_{\text{PID}}^i$ (with i being the particle identity under study). Below $p_T = 0.5$ GeV/c, only the TPC information is used ($n\sigma_{\text{PID}}^i = n\sigma_{\text{TPC}}^i$). For larger p_T, the TPC and TOF information is combined using a geometrical mean: $n\sigma_{\text{PID}}^i = \sqrt{(n\sigma_{\text{TPC}}^i)^2 + (n\sigma_{\text{TOF}}^i)^2}$. Tracks are required to be within $3\sigma_{\text{PID}}$ of the expected value to be identified as $\pi^\pm$, $K^\pm$, or p $(\overline{p})$. In the region where the $3\sigma_{\text{PID}}$ identification bands of two species overlap, the identity corresponding to the smaller $n\sigma_{\text{PID}}$ is assigned. This technique gives a good track-by-track identification in the following p_T ranges: $0.2 < p_T < 4$ GeV/c for $\pi^\pm$, $0.3 < p_T < 3.2$ GeV/c for $K^\pm$, $0.5 < p_T < 4$ GeV/c for p $(\overline{p})$. The misidentification of tracks is below 4% for pions, 25% for kaons, and 10% for protons in those ranges. Further discussion on the ALICE particle identification (PID) performance can be found in Refs. [26,38]. The results for identified particles are provided in the pseudorapidity range $0.5 < |\eta| < 0.8$. However, in the case of the q_2^{V0C} selection the results were also studied at midrapidity $|y| < 0.5$. Results for positive and negative particles are consistent. In the following, "pions," "kaons," and "protons," as well as the symbols "π," "K," and "p," refer to the sum of particles and antiparticles.

The results for the spectra in ESE-selected events are presented in terms of ratios between the distributions measured in the large-q_2 (small-q_2) samples and the unbiased sample. The unbiased spectra have already been reported in Refs. [37,38]. Most of the corrections (and uncertainties) cancel out in these ratios, allowing for a precise determination of the effect owing to the event-shape selection, as discussed in detail below. The uncertainties can mostly arise owing to effects that depend on the local track density, which are found to be small [39].

The systematic uncertainties are summarized in Tables III and IV. As mentioned before, only the checks and variations that are found to be statistically significant are considered in the systematic uncertainties [36].

TABLE III. Summary of systematic errors for the ratio of p_T distributions between large-q_2 and unbiased events. NS, not statistically significant.

Effect	N_{ch}	$\pi^\pm$	$K^\pm$	p and $\bar p$
Track reconstruction	<0.035%	0.07%	0.07%	0.07%
Tracking efficiency	0.21%	0.21%	0.21%	0.21%
Centrality resolution	0.07% ($p_T > 1.5$ GeV/c)	0.07% ($p_T > 1.5$ GeV/c)	0.14%	0.14%
Centrality estimator	0.35%	0.35%	0.35%	0.35%
PID	–	0.07% ($p_T > 1.5$ GeV/c)	0.07%	0.07%
Secondary particles	<0.035%	<0.035%	<0.035%	0.07%
Normalization	1.1%	1.1%	1.1%	1.1%
Magnetic field	NS	NS	NS	NS
Charge	<0.035%	<0.035%	<0.035%	<0.035%
Vertex	0.07%	0.07%	0.07%	0.07%

TABLE IV. Summary of systematic errors for the ratio of p_T distributions between small-q_2 and unbiased events. NS, not statistically significant.

Effect	N_{ch}	$\pi^{\pm}$	$K^{\pm}$	p and $\bar{p}$
Track reconstruction	<0.035%	0.07%	0.07%	0.07%
Tracking efficiency	0.28%	0.28%	0.28%	0.28%
Centrality resolution	0.07% ($p_T > 1.5$ GeV/c)	0.07% ($p_T > 1.5$ GeV/c)	0.14%	0.14%
Centrality estimator	0.35%	0.35%	0.35%	0.35%
PID	–	0.07% ($p_T > 1.5$ GeV/c)	0.07%	0.07%
Secondary particles	<0.035%	<0.035%	<0.035%	0.07%
Normalization	0.6%	0.6%	0.6%	0.6%
Magnetic field	NS	NS	NS	NS
Charge	<0.035%	<0.035%	<0.035%	<0.035%
Vertex	0.07%	0.07%	0.07%	0.07%

The systematic uncertainty related to the tracking is estimated varying the track selection cuts. Instead of the standard TPC cluster cut, at least 120 (of 159) pad-row hits in the TPC and a fraction of shared clusters in the TPC <0.4 are required (*track reconstruction* in Tables III and IV).

The possible effect of a track-density-dependent efficiency (which would influence in a different way events with the large- and small-q_2 selection) is investigated using simulations based on the AMPT event generator [33] and a parametric event generator tuned to reproduce the ALICE spectra and v_2 measurements [39]. This effect leads to an uncorrelated systematic error of about 0.2% and a normalization error of 0.4% (*tracking efficiency*).

The uncertainty on the centrality is estimated varying the definitions of centrality classes by 1% and using tracks as the centrality estimator. These checks lead to an uncorrelated uncertainty of about 0.1% and 0.35%, respectively, and a normalization uncertainty below 1% in the ratios of spectra (*centrality resolution* and *centrality estimator*).

The systematic effect related to the particle identification is studied performing several variations to the PID approach described above. The $n\sigma_{\mathrm{PID}}$ cut is varied between 2 and 4. Alternatively, if a track is consistent with more than one particle assignment within the $n\sigma_{\mathrm{PID}}$ cut, double counting is allowed. As compared to the standard strategy where only the identity closest to the measured $n\sigma_{\mathrm{PID}}$ is selected, this approach leads to a slightly larger contamination from misidentified tracks, but also to a larger efficiency. Finally, an exclusive $n\sigma_{\mathrm{PID}}$ strategy was used, which drastically reduces misidentification: a particle is accepted only if it is compatible with only one mass hypothesis at $3\sigma_{\mathrm{PID}}$. As a further cross-check, a Bayesian approach [26] was also considered. This method allows for better control of contamination at high p_T. Overall, the uncertainty related to the particle identification strategy is less than 0.1% (*PID*).

The effect of secondary particles depends on the p_T distribution of weakly decaying primary particles, and could be different for the large- and small-q_2 samples. This effect is estimated to be at most $\sim$0.1% for protons with the TPC ESE selection and negligible in all other cases (*secondary particles*).

Possible effects related to the magnetic field and to the charge state are addressed studying separately events collected with different magnet polarities (*magnetic field*) and different charges (*charge*), as in the case of the $v_2\{\mathrm{SP}\}$ measurement. Particles produced at different longitudinal position cross a different portion of the detector, with different reconstruction efficiency. The samples of events produced with a negative ($-10 < z_{\mathrm{vtx}} < 0$ cm) and positive ($0 < z_{\mathrm{vtx}} < 10$ cm) longitudinal vertex coordinate with respect to the nominal interaction point were studied separately (*vertex*).

IV. RESULTS

A. Charged-particle elliptic flow

The event-shape selection is studied in Fig. 3, where the $v_2\{\mathrm{SP}\}$ as a function of p_T is reported for the unbiased and ESE-selected samples, with both the q_2^{TPC} ($|\eta| < 0.4$) and q_2^{V0C} ($-3.7 < \eta < -1.7$) selections in different centrality classes. Figure 4 shows the ratio between the v_2 measured with the large-q_2 (small-q_2) selection and the unbiased sample. Selecting the 10% highest (lowest) q_2^{TPC} samples leads to a change of 30%–50% in the $v_2\{\mathrm{SP}\}$ measured, depending on centrality. The change is smaller ($\sim$10%–25%) in the case of q_2^{V0C}-based selection, as compared to the q_2^{TPC} case. As already indirectly inferred from the difference between second- and fourth-order flow cumulants $v_2\{2\}$ and $v_2\{4\}$ in Ref. [12], the elliptic flow response of the system to geometry fluctuations is almost independent of p_T. For all centralities, the change observed in Fig. 4 depends indeed weakly on p_T, up to at least 4–5 GeV/c. This indicates that a cut on q_2 selects a global property of the event, likely related to the initial shape in the overlap region. The only exception to the previous observation is the 0%–5% centrality class, where for the q_2^{TPC} selection an increasing trend with p_T is observed. In this centrality class the mean value of v_2 is small, owing to the almost isotropic shape in the initial state. Moreover, relative flow fluctuations are large in central collisions, with a p_T dependence similar to the one shown in Fig. 4 [12]. The analysis of the p_T spectra presented in Sec. IV B gives additional insight into the trend observed in Fig. 4.

For $p_T \gtrsim 4$–5 GeV/c, the ratio ESE-selected/unbiased $v_2\{\mathrm{SP}\}$ increases for the large-q_2 selection. This trend is more pronounced for the q_2^{TPC} selection and for the most central and the most peripheral classes. A fit with a constant over the full p_T range yields χ^2 per degree of freedom values in the
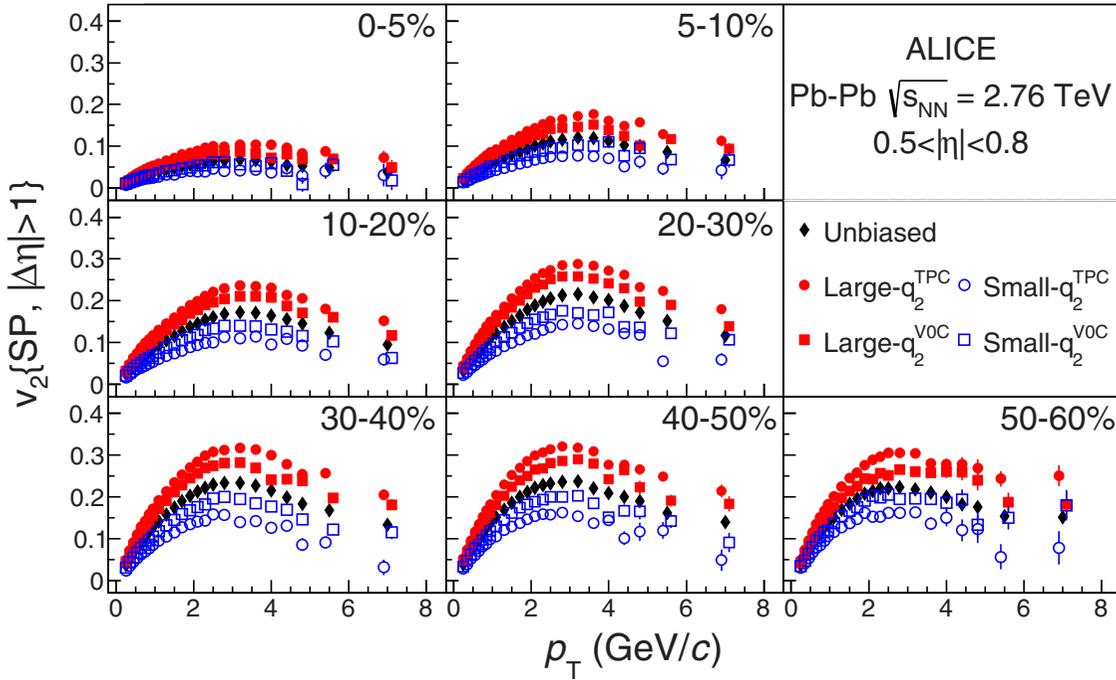
FIG. 3. Measurement of $v_2\{SP\}$ as a function of p_T in different centrality classes for the unbiased, the large-q_2 and the small-q_2 samples. Only statistical uncertainties are plotted (systematic uncertainties are smaller than the markers).

range 2–6 (depending on centrality) for the q_2^{TPC} selection and <2 for the q_2^{V0C} selection. Fitting the ranges $p_T < 5$ GeV/c and $p_T > 5$ GeV/c with two different constants indicates an increase for the large-q_2 selection of order 5% and 10% for the q_2^{V0C} and q_2^{TPC} selections, respectively. This difference could be attributable to a small nonflow-induced bias. At high p_T the

v_2 is believed to be determined by the path-length dependence of parton energy loss [12].

The difference between the q_2^{TPC} and q_2^{V0C} is attributed to the different selectivity (see Sec. III A), but also to a different contribution of nonflow correlations between the q_2 and the v_2 measurements. Replacing the q_2^{TPC} selection with the q_2^{V0C}
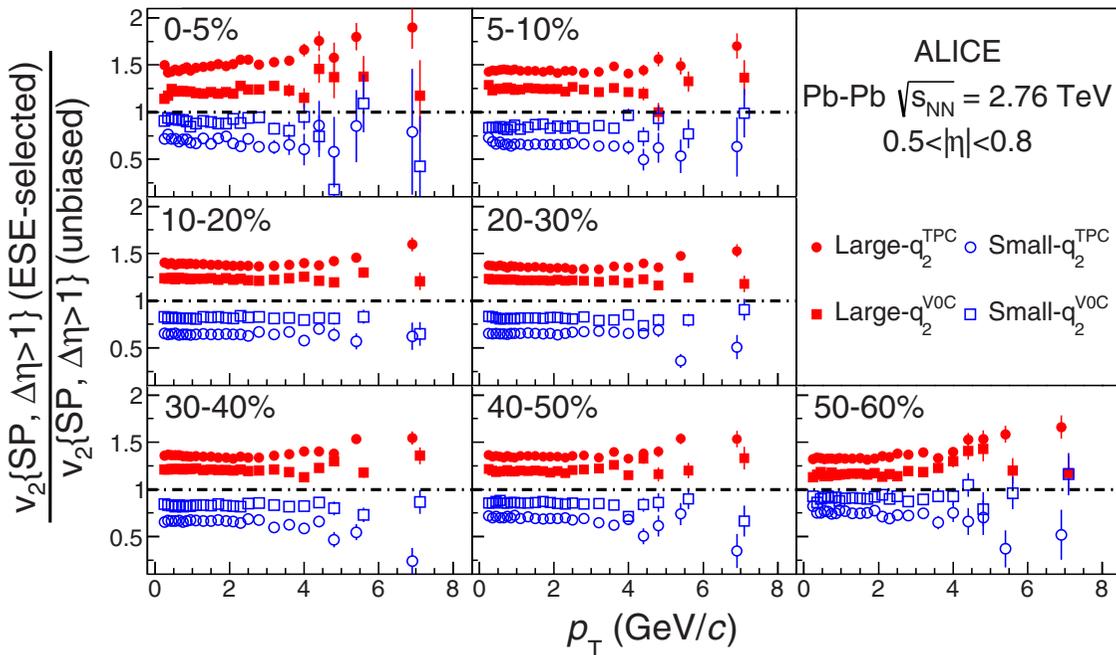
FIG. 4. Ratio of $v_2\{SP\}$ in the large-q_2 and small-q_2 samples to unbiased sample. Only statistical uncertainties are plotted (systematic uncertainties are smaller than the markers).
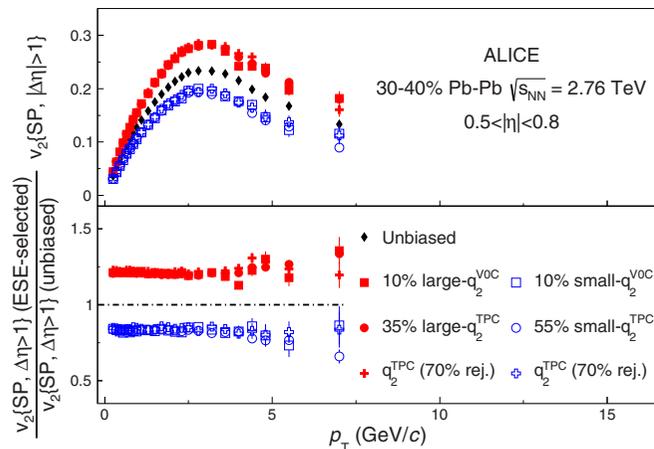
FIG. 5. Comparison between the effect of the event-shape selection obtained with the standard V0C and with the tuned TPC selections (see text for details), in the centrality class 30%–40%. (Top) $v_2\{SP\}$; (bottom) ratios to the unbiased sample. Only statistical uncertainties are plotted (systematic uncertainties are smaller than the markers).

FIG. 6. Centrality dependence of the average $v_2\{SP\}$ variation in the large-q_2 and small-q_2 samples.

one changes both nonflow and selectivity at the same time. To disentangle these two contributions, the selectivity of the q_2^{TPC} selection was artificially reduced. This is achieved either relaxing the selection itself or rejecting a random fraction of tracks for the computation of q_2^{TPC}, while still selecting 10% of the events. It is found that selecting the class 65%–100% for the large-q_2 sample (0%–55% for the small-q_2 sample) with q_2^{TPC}, or alternatively rejecting 70% of the TPC tracks, leads to an average variation of the $v_2\{SP\}$ in the range $0.2 < p_T < 4$ GeV/c comparable to the one obtained with the standard 10% q_2^{V0C} selection. The results are shown in Fig. 5 for the centrality class 30%–40%. Not only is it possible to find a cut which leads to the same average variation in $v_2\{SP\}$, but the p_T dependence is very similar in both cases. Rejecting randomly 70% of the tracks changes the selectivity of q_2^{TPC} without affecting nonflow correlations between the q_2^{TPC} selection and $v_2\{SP\}$ measurement (as the η gap is not varied). Also in this case, it is found that the effect of the q_2 selection does not depend on p_T. A similar result, with the same value of the relaxed cut or fraction of rejected tracks, is found for the centrality interval 10%–50%. Moreover, as discussed in the next section, the same relaxed selections lead to the same effect on the p_T distributions.

These checks demonstrate that the selectivity of the cut is the main reason for the difference between the TPC and V0C selections. Owing to the large η gap, the nonflow contribution is expected to be negligible in the case of the q_2^{V0C} selection. The agreement observed in Fig. 5 indicates that, in the centrality classes 10%–50%, this is also the case for the q_2^{TPC} selection in the range $p_T < 5$ GeV/c, a transverse momentum region dominated by hydrodynamic effects [38]. It is worth noticing that the ATLAS Collaboration measured a modification of the elliptic flow of ~35%, nearly independent of p_T up to ~12 GeV/c in the 20%–30% centrality class, while measuring v_2 and q_2 with a pseudorapidity gap of 0.7
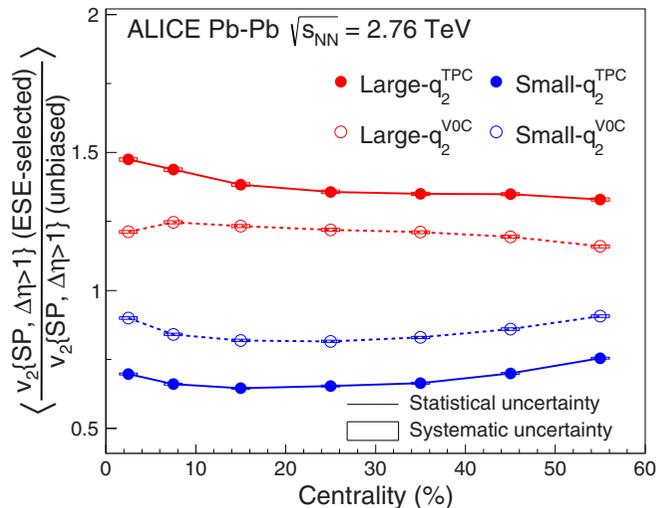
units [23]. The increasing trend in the centrality class 0%–5% is also observed in Ref. [23].[1]

To study the centrality and the q_2 dependence of $v_2\{SP\}$ in ESE-selected event classes, we quantified the average change for each centrality class fitting the ratios in the range $0.2 < p_T < 4$ GeV/c with a constant.[2] The centrality dependence of the average change in the large-q_2 and small-q_2 selection is reported in Fig. 6. The trend obtained with the q_2^{TPC} and q_2^{V0C} selections is very similar, except for the most central class 0%–5%, where the average is influenced by the nonflat trend seen in Fig. 4. This once again reinforces the conclusion that the nonflow contamination is small also in the TPC selection case for the bulk of particles. The relative importance of nonflow changes with centrality. A large nonflow bias would therefore introduce a centrality dependence in the relative trend between the q_2^{TPC} and the q_2^{V0C} selections, which is not observed. The dependence of the $v_2\{SP\}$ variation on q_2^{TPC} and q_2^{V0C} is shown for the centrality classes 5%–10%, 30%–40%, and 50%–60% in Fig. 7. The left panel shows the absolute q_2 values on the x axis, while the right panel depicts the self-normalized values, defined as the average q_2 value in ESE-selected events over the average q_2 values for all events in a given centrality class. The V0C selection spans a larger range but the TPC is more selective, as is clearly seen from the different slope of the TPC and V0C curves. In both cases the average q_2 reaches values twice as large compared to those in the unbiased sample (Fig. 7, right).

In summary, the observations reported in this section indicate that the ESE selects a global property of the collisions, as suggested by the flat modification in the v_2 as a function of p_T. The q_2^{TPC} leads to a change twice as large than the

---

[1]See auxiliary figures available on the ATLAS Collaboration web page https://atlas.web.cern.ch/Atlas/GROUPS/PHYSICS/PAPERS/HION-2014-03/.

[2]The result of the fit is numerically equivalent to the direct computation of the integrated v_2 in the range $0.2 < p_T < 20$ GeV/c.
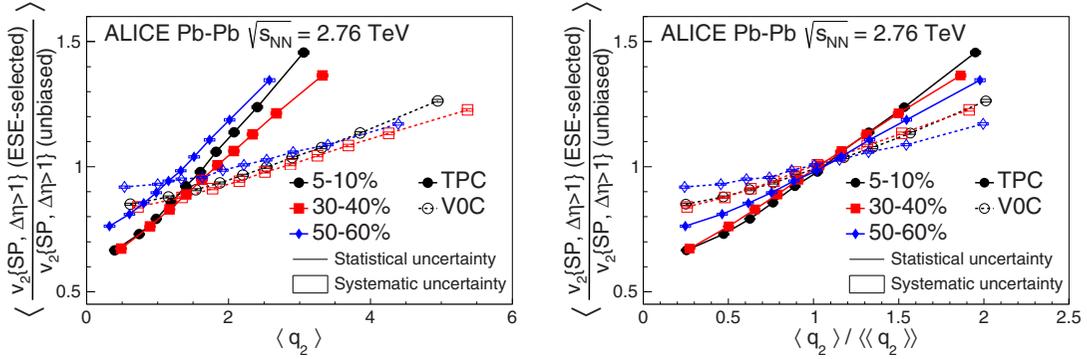
FIG. 7. Average $v_2\{SP\}$ variation as a function of the absolute (left) values and self-normalized (right) values of the q_2^{TPC} and q_2^{V0C} for several centrality classes.

corresponding q_2^{V0C} selection. The difference between the two seems to be mostly attributable to the different discriminating power rather than to nonflow effects.

B. Transverse momentum distributions

To study the interplay between the initial configuration of the system and the dynamics of the expansion of the fireball, the effect of the ESE selection on the single particle p_T distribution is reported in Fig. 8, for the q_2^{TPC} and q_2^{V0C} selections. As discussed in Sec. III A, the reduced flow vector is calculated in the TPC detector in the pseudorapidity range $|\eta| < 0.4$. To avoid overlap between the q_2^{TPC} and p_T distribution measurements, only the region $0.5 < |\eta| < 0.8$ is used to measure the p_T distributions. This ensures at least 0.1 units of pseudorapidity separation between the q_2 and spectra measurements, thus suppressing the effect of short-

range correlations. For consistency with the TPC analysis, the same pseudorapidity range is used in the case of the V0C selection. In the q_2^{V0C} case, it is also possible to study the spectra at midrapidity $|\eta| < 0.8$ without any overlap with the q_2 measurement. The results agree within uncertainty with those in $0.5 < |\eta| < 0.8$.

The spectra in the large-q_2 sample are harder than those in the small-q_2 one. The ratio to the unbiased spectra reaches a maximum around $p_T = 4$ GeV/c and then stays approximately constant within large uncertainties.

The effect of the selection is more pronounced in semi-central events ($\sim 30\%$–50%) and decreases both towards more central and more peripheral collisions. This can be attributable to the fact that the q_2 spans a larger dynamic range in semicentral collisions (Figs. 1 and 7). In the most peripheral centrality class studied in this paper (50%–60%) the effect of the TPC-based selection is still very pronounced, while
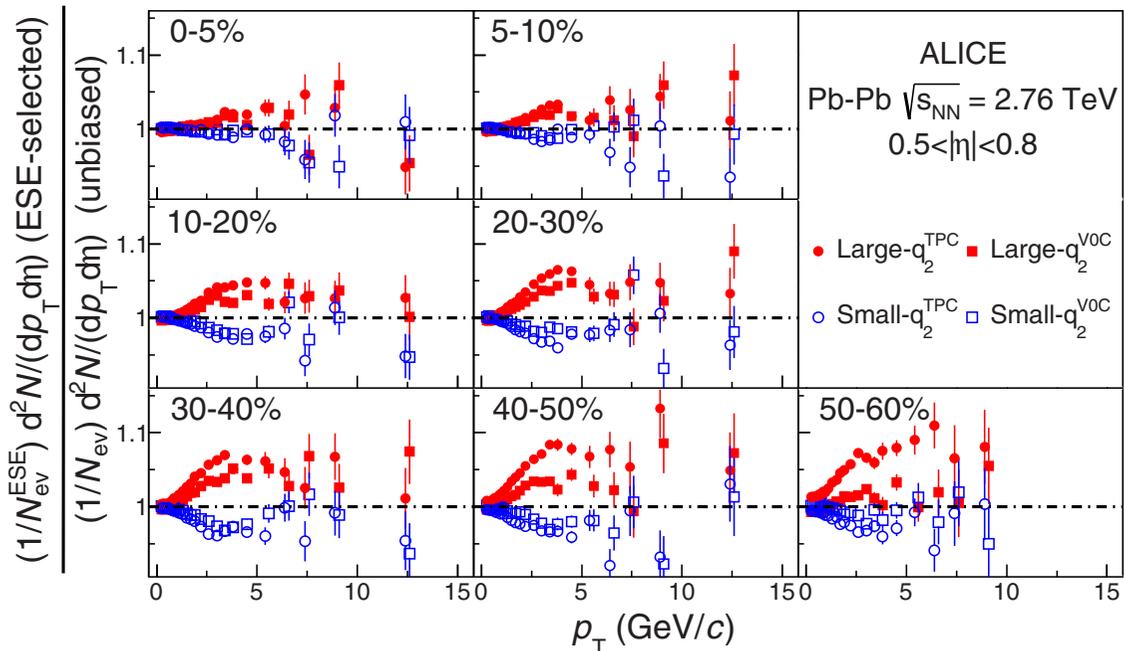

FIG. 8. Ratio of the p_T distribution of charged hadrons in the large-q_2 or small-q_2 sample to the unbiased sample (q_2^{V0C} and q_2^{TPC} selections) in different centrality classes. Only statistical uncertainties are plotted (systematic uncertainties are smaller than the markers).
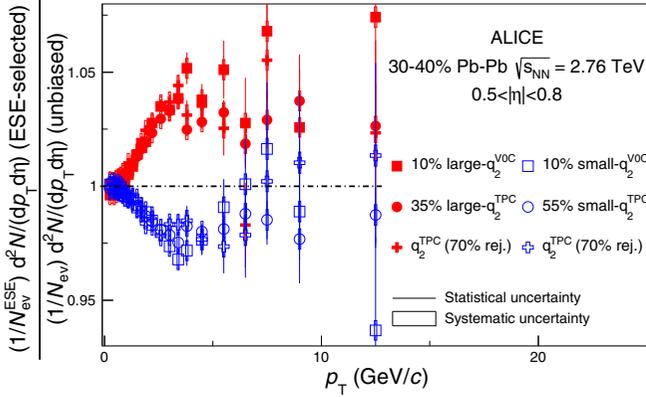
FIG. 9. Ratio of the p_T distribution of charged hadrons in the large-q_2 or small-q_2 sample to the unbiased sample. Comparison between the effect of the event-shape selection obtained with the standard V0C and with the tuned TPC selections (see text for details), in the centrality class 30%–40%.

the q_2^{V0C} selection is less effective. This may indicate a small contamination from nonflow effects in the most peripheral class, consistent with observations discussed for the $v_2\{\mathrm{SP}\}$ measurement in Sec. IV A. In the most central class (0%–5%) the modification of the spectrum is very small. This suggests that the trend observed in the same centrality class in Fig. 4 is likely to be dominated by flow fluctuations rather than nonflow contributions.

As in the previous section, we disentangle the effect of nonflow and q_2 selectivity either relaxing the q_2^{TPC} selection or randomly rejecting a fraction of the tracks. The relaxed cut and the fraction of rejected tracks tuned to reproduce the v_2 variation in $0.2 < p_T < 4$ GeV/c in Sec. IV A are used. Figure 9 shows that these selections yield results compatible with the standard q_2^{V0C} selection. A similar result (with the same relaxed cuts or fraction of rejected tracks) is found for all centralities up to $\sim$50%, after which nonflow effects seem to become relevant.

As discussed in Sec. IV A, we conclude that the effect of nonflow is small and that the main factor driving these observations is the average v_2 at midrapidity.

The modification on the spectra of identified π, K, and p is reported in Figs. 10 and 11 for different centrality classes. The same pattern measured in the case of nonidentified hadrons is observed. Moreover, a clear mass ordering is seen: the modification is more pronounced for heavier particles. Conversely, the spectra in the small-q_2 sample are softer. In the case of the V0C selection the analysis was also repeated in the region $|y| < 0.5$, yielding consistent results.

These observations suggest that the spectra in the large-q_2 (small-q_2) sample are affected by a larger (smaller) radial flow push. This hypothesis was tested with a blast-wave [40] study. A ratio of two blast-wave functions was used to fit the spectra ratios shown in Figs. 10 and 11. The parameters were initially fixed to the values from Ref. [38], where they were tuned to describe the inclusive spectra of pions, kaons, and protons. Then, the $\langle\beta_T\rangle$ parameter of the numerator function was allowed to change (while keeping the overall integral of the

function constant). The fit was performed as in Ref. [38] in the transverse momentum ranges 0.5–1, 0.2–1.5, and 0.3–3 GeV/c for π, K, and p, respectively. The agreement with the data is good, also outside the range used to determine the parameters, up to $p_T \sim 3$ GeV/c. The fits yield the following result for the difference $\Delta\langle\beta_T\rangle$ between the $\langle\beta_T\rangle$ parameter of the numerator and denominator function: $\Delta\langle\beta_T\rangle = (0.41 \pm 0.03)\%$ (large-q_2) and $\Delta\langle\beta_T\rangle = (-0.22 \pm 0.03)\%$ (small-q_2) for the centrality class 30%–40%, as shown in Fig. 12.

V. DISCUSSION

In this paper the first application of the ESE [20] to the analysis of ALICE data was presented.

The results on the $v_2\{\mathrm{SP}\}$ measurement suggest that the ESE technique selects a global property of the collision, likely related to the eccentricity in the initial state. The measurement of p_T spectra indicates that events with larger eccentricity show an increased radial flow. A correlation between elliptic and radial flow could be introduced either at the initial stage, owing to the specific fluctuation patterns in the energy deposition, or during the hydrodynamic evolution of the system, owing to an interplay of bulk and shear viscosity [7].

A Glauber Monte Carlo simulation was performed to estimate the possible correlation between the initial eccentricity and azimuthally averaged pressure gradients. In the model, the multiplicity of charged particles in the acceptance of the V0 detector, used to determine the centrality classes, is computed following Ref. [29]. A "number of ancestors" $N_{\mathrm{ancestors}}$ is derived from the number of participant nucleons (N_{part}) and binary collisions (N_{coll}) as

$$N_{\mathrm{ancestors}} = f N_{\mathrm{part}} + (1 - f) N_{\mathrm{coll}}. \qquad (6)$$

Each ancestor is assumed to produce particles following a negative binomial distribution with parameters taken from Ref. [29].

The participant density, defined following Refs. [9,41–43] as N_{part}/S, is used as a proxy for the average pressure gradients. The average cross-sectional area S and participant eccentricity ϵ are computed as

$$S = 4\pi \sigma_{x'}\sigma_{y'} = 4\pi \sqrt{\sigma_x^2 \sigma_y^2 - \sigma_{xy}^2}, \qquad (7)$$

$$\epsilon = \frac{\sigma_{y'}^2 - \sigma_{x'}^2}{\sigma_{x'}^2 + \sigma_{y'}^2} = \frac{\sqrt{\left(\sigma_y^2 - \sigma_x^2\right)^2 + 4\sigma_{xy}^2}}{\sigma_x^2 + \sigma_y^2}, \qquad (8)$$

where

$$\sigma_x^2 = \langle x^2\rangle - \langle x\rangle^2, \ \ \sigma_y^2 = \langle y^2\rangle - \langle y\rangle^2, \ \ \sigma_{xy} = \langle xy\rangle - \langle x\rangle\langle y\rangle. \qquad (9)$$

The unprimed coordinates are given in the fixed laboratory coordinate frame. Primed coordinates, x' and y', are calculated in the so-called participant coordinate system, rotated with respect to the laboratory coordinate frame such that the minor symmetry axis of the participant nucleon distribution coincides with the x' direction. The normalization of the area is chosen such that for a Gaussian distribution the *average* density coincides with N_{part}/S.
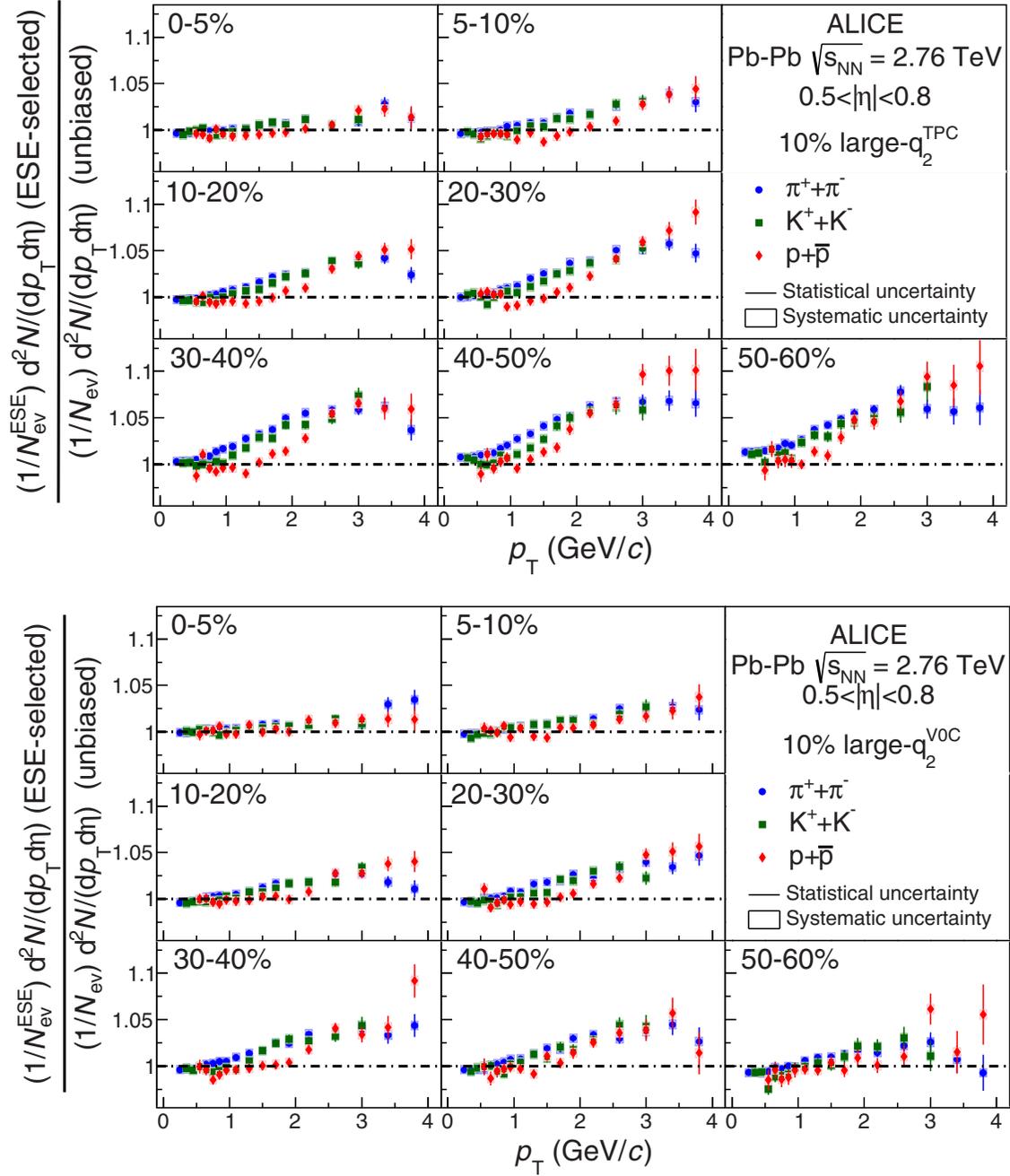
FIG. 10. Ratio of the p_T distribution of identified charged hadrons in the large-q_2 sample to the unbiased sample for the q_2^{TPC} (top) and q_2^{V0C} (bottom) selections.

Two narrow centrality classes, selected based on the simulated charged particle multiplicity, roughly corresponding to 0%–2% (central) and 30%–32% (semicentral), are studied in Fig. 13. The observed correlation between the density and the participant eccentricity is reminiscent of the correlation between radial flow and event shape measured in this paper. The average density in events with the 10% largest ϵ is about 1% (7%) larger than in events with the smallest ϵ for central (semicentral) collisions, qualitatively consistent with what is observed in Figs. 10 and 11, where the effect of the ESE selection is much stronger for semicentral collisions. This

reinforces our conclusion that ESE is an effective tool to select the initial shape and density, thereby opening the possibility of further studies.

A quantitative comparison would require a full hydrodynamical calculation. The correlation can, in fact, be modified by the transport in the hydrodynamic phase. In particular, it was shown [7,44] that in a system with a finite shear viscosity the flow coefficients, obtained for a given set of initial eccentricities, are reduced as compared to the ideal hydrodynamics case. At the same time, shear viscosity increases the radial flow. In principle, bulk viscosity reduces the radial flow, reducing
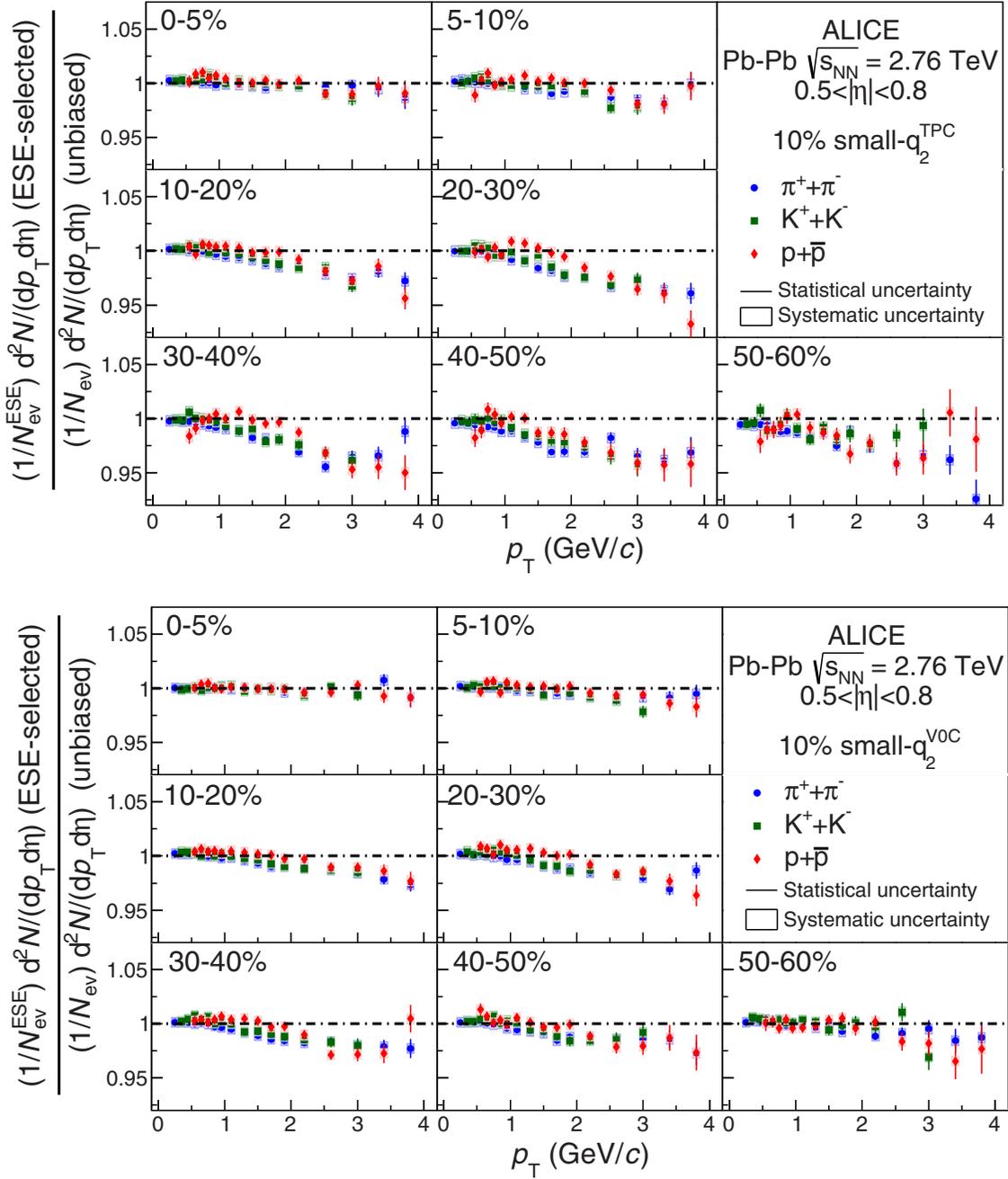
FIG. 11. Ratio of the p_T distribution of identified charged hadrons in the small-q_2 sample to the unbiased sample for the q_2^{TPC} (top) and q_2^{V0C} (bottom) selection.

the correlation observed in this paper, but the latter effect was estimated to be negligible [44]. Therefore, the measurement we present in this paper is sensitive to the interplay of initial conditions and transport coefficients in the hydrodynamic phase. As such, it poses stringent constraints on hydrodynamic calculations, and it could allow the extraction of the value of average shear viscosity at the LHC.

A study of the relation of the fluctuation in the initial size to the spectra was performed in Refs. [45,46] with a full hydrodynamic simulation. It was shown that the event-by-event fluctuations in the Glauber initial conditions lead

to fluctuations in the initial size of the system that reflect in fluctuations of the radial flow and hence ⟨p_T⟩. It is found that the relative ⟨p_T⟩ fluctuations computed with Glauber initial conditions overestimate the data, indicating a strong sensitivity of event-by-event measurements on the initial conditions model. It is also shown that the ⟨p_T⟩ fluctuations are not sensitive to the shear viscosity. The study in Refs. [45,46] (fluctuations in ⟨p_T⟩), however, does not address the relation between the elliptic and the radial flows. It may be expected that the present measurement will also be sensitive to the transport coefficient of the medium.
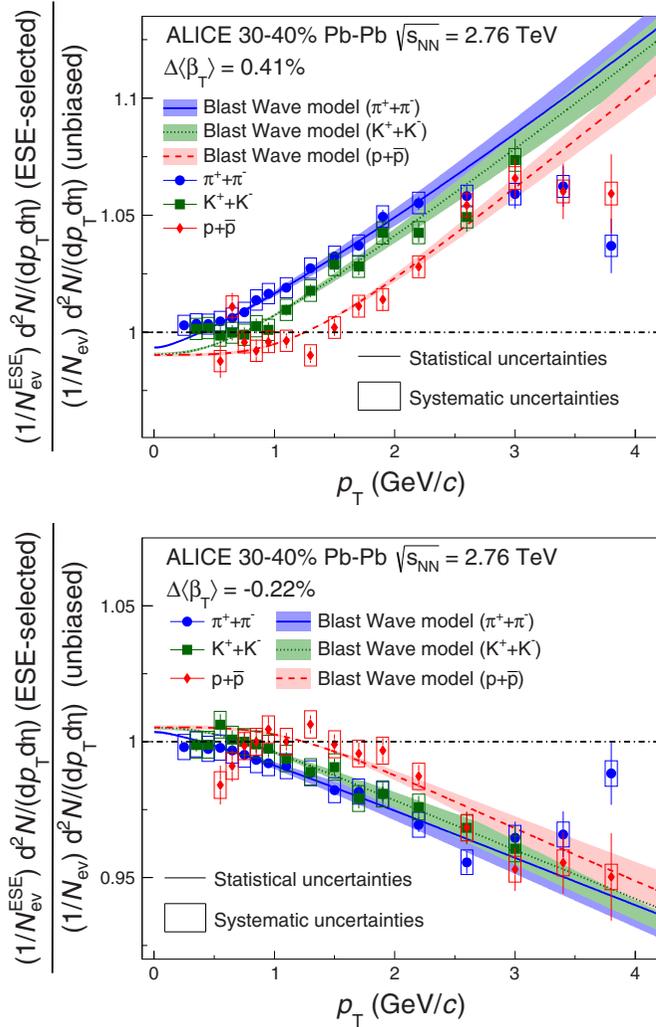
FIG. 12. Ratio of the p_T distribution of identified charged hadrons in the large-q_2 (top) and small-q_2 (bottom) sample to the unbiased sample (q_2^{TPC} selection), in 30%–40% centrality class. Lines: ratio of the blast-wave parametrizations (see text for details).

FIG. 13. Participant density as a function of the participant eccentricity estimated in a Glauber Monte Carlo model for central (top) and semicentral (bottom) collisions.

In a recent series of theoretical studies [47–49], it was suggested to use the principal component analysis (PCA) to study flow fluctuations. It was argued that most of the current methods to study flow do not fully capture the complexity of the initial state. Indeed, the PCA studies revealed the presence of subleading flow components (arising from radial geometry excitations), which break the factorization of flow harmonics [47,48], In particular, in Ref. [49] it is argued that the subleading component of v_2 reflects a nonlinear mixing with radial flow, which could address the same physics as reported in this paper.

To further understand the observed effect, we studied it in AMPT, a model known to reproduce many of the flow observables measured at the LHC [33]. This model is based on HIJING [50] to describe the initial conditions and on the Zhang's parton cascade [51] to describe the partonic evolution. The *string melting* configuration, described in Ref. [52], is used. To assess the impact of the detector resolution on the
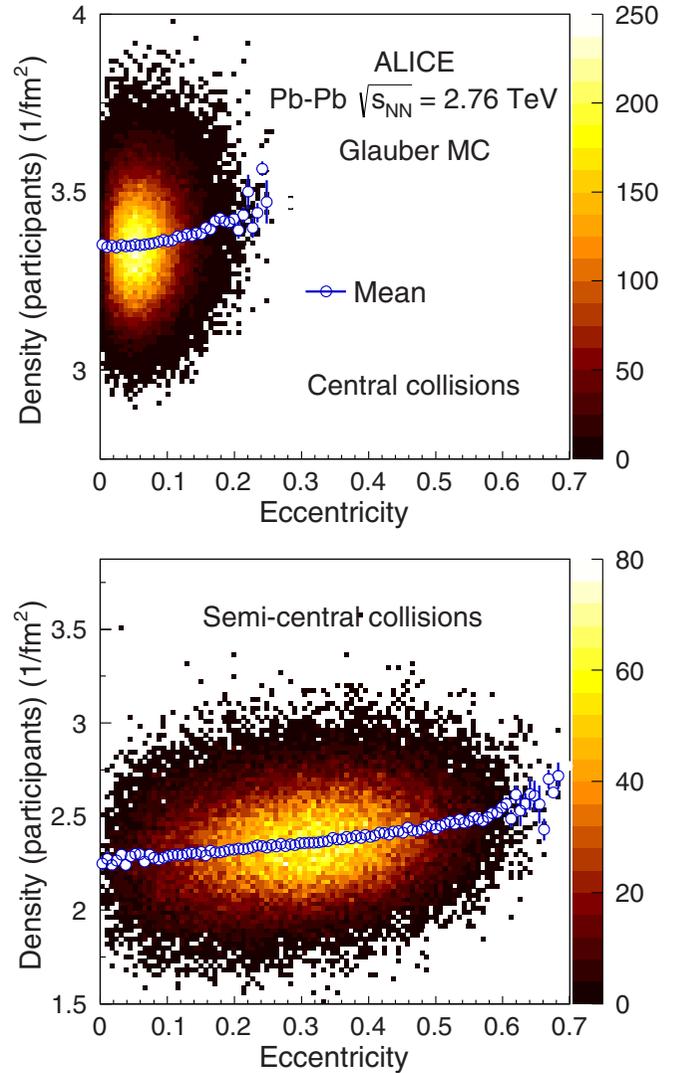
q_2 selection, the simulated AMPT events were transported through the ALICE apparatus using the GEANT [34] transport model. The q_2 was computed in $|\eta| < 0.4$ using either the reconstructed Monte Carlo tracks (q_2^{rec}) or the generated primary particles in the same kinematic range (q_2^{gen}). The elliptic flow and the transverse momentum distribution are calculated using generated Monte Carlo particles. Because the charged-particle multiplicity distribution is different in AMPT and data, the q_2 selection is calibrated in the model as a function of multiplicity. The results are shown in Fig. 14 for the charged-hadron elliptic flow and in Fig. 15 for the transverse momentum distribution of charged hadrons. Using either q_2^{rec} or q_2^{gen} does not introduce any significant difference on the effect of the selection. This indicates that detector resolution effects are negligible for the q_2^{TPC} selection. The V0 detectors, however, have a coarser azimuthal resolution and are sensitive to fluctuations in the energy deposition of incident particles. However, the study with the relaxed TPC selection discussed
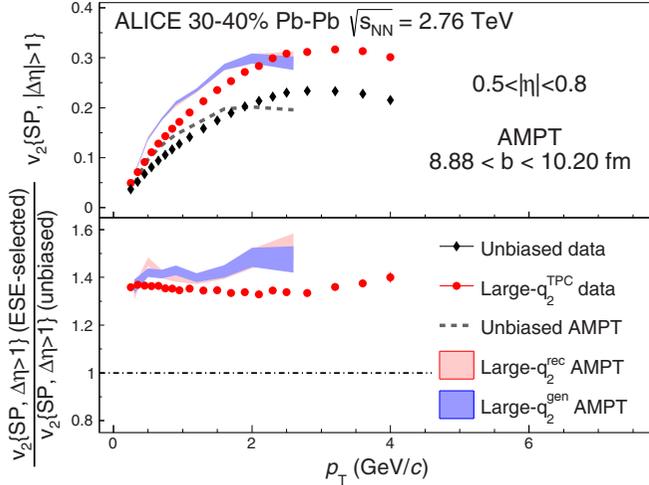
FIG. 14. Measurement of $v_2\{SP\}$ as a function of p_T, for the unbiased sample and for the large-q_2 sample (top) and ratio between the large-q_2 result over the unbiased result (bottom). Data points (solid markers) are compared with AMPT Monte Carlo model (bands). Only statistical uncertainties are plotted (systematic uncertainties are smaller than the markers).

in Sec. IV demonstrates that the properties of the ESE-selected events are mostly determined by the average $v_2\{SP\}$ value. It is therefore advised that in any comparison of this data to theoretical models the selection in the model is tuned as to reproduce the average change in $v_2\{SP\}$ at midrapidity.

The p_T dependence of the elliptic flow observed in data is not reproduced in AMPT (top panel). This model reproduces, however, the magnitude of the modification, as well as the flatness of the ratio as a function of p_T.

The effect of the ESE selection on the p_T distribution of charged particles is well reproduced by AMPT below $p_T = 2\,\mathrm{GeV}/c$, as shown in Fig. 15. However, the magnitude of the effect at intermediate p_T ($2 < p_T < 6\,\mathrm{GeV}/c$) is underestimated in AMPT. As previously observed for the

v_2 measurement, a good agreement is observed between the selection based on q_2^{gen} and q_2^{rec}.

VI. CONCLUSIONS

In summary, the first application of the ESE technique to Pb-Pb collision data measured by ALICE at $\sqrt{s_{NN}} = 2.76\,\mathrm{TeV}$ has been presented.

The elliptic flow at midrapidity is observed to increase as a function of the q_2 calculated in the central or forward rapidity regions. The modification of the v_2 coefficient as a function of p_T is nearly flat below $p_T = 4\,\mathrm{GeV}/c$, suggesting that this technique allows the selection of a global property of the collision, likely related with the geometry of the participant nucleons in the initial state. In the region above $p_T > 5\,\mathrm{GeV}/c$ a small increase is observed within the large statistical uncertainties, possibly owing to a small nonflow contamination. In this transverse momentum range the elliptic flow is believed to be driven by the different path length traversed in and out of plane by high-p_T partons in the deconfined medium, rather than by the hydrodynamic evolution of the system.

The p_T distributions of unidentified hadrons in the p_T region ($0 < p_T < 5\,\mathrm{GeV}/c$) are harder (softer) in events with large-q_2 (small-q_2) values.

Identified pions, kaons, and protons show a similar behavior with a clear mass ordering in the ratio between the large-q_2 and the unbiased spectra, thus suggesting this effect to be attributable to a stronger radial flow in such events. Glauber Monte Carlo calculations reveal a correlation between the transverse participant density and the participant eccentricity which could be the origin of this effect. This indicates that at least part of the correlation is generated in the initial state. However, these measurements are also sensitive to the transport coefficients in the hydrodynamic evolution. A quantitative comparison would require a full hydrodynamic calculation and may provide stringent constraints on both shear and bulk viscosity.
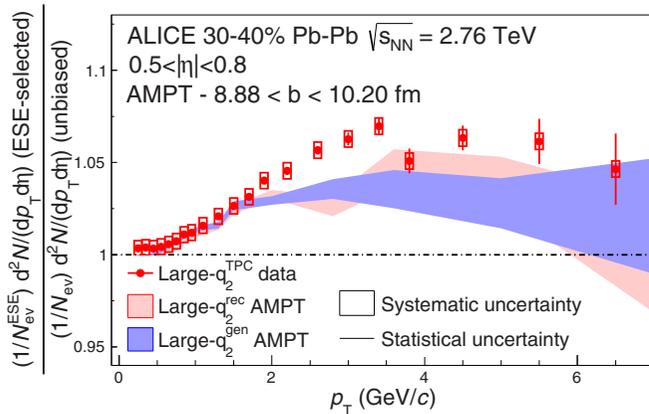
FIG. 15. Ratio of the p_T distribution of charged hadrons in the large-q_2 sample to the unbiased sample for the q_2^{TPC} selection. Data points (solid markers) are compared with AMPT Monte Carlo model (bands).

[1] S. Borsanyi *et al.* (Wuppertal-Budapest Collaboration), Is there still any T_c mystery in lattice QCD? Results with physical masses in the continuum limit III, J. High Energy Phys. 09 (2010) 073.

[2] A. Bazavov, T. Bhattacharya, M. Cheng, C. DeTar, H. Ding *et al.*, The chiral and deconfinement aspects of the QCD transition, Phys. Rev. D **85**, 054503 (2012).

[3] N. Armesto, N. Borghini, S. Jeon, U. Wiedemann, S. Abreu *et al.*, Heavy ion collisions at the LHC-Last call for predictions, J. Phys. G **35**, 054001 (2008).

[4] J. Schukraft, Heavy ion physics at the LHC: What's new? What's next?, Phys. Scr. **T158**, 014003 (2013).

[5] Y. Akiba, A. Angerami, H. Caines, A. Frawley, U. Heinz *et al.*, The hot QCD white paper: Exploring the phases of QCD at RHIC and the LHC, arXiv:1502.02730 [nucl-ex].

[6] C. Gale, S. Jeon, and B. Schenke, Hydrodynamic modeling of heavy-ion collisions, Int. J. Mod. Phys. A **28**, 1340011 (2013).

[7] U. Heinz and R. Snellings, Collective flow and viscosity in relativistic heavy-ion collisions, Annu. Rev. Nucl. Part. Sci. **63**, 123 (2013).

[8] G. Aad *et al.* (ATLAS Collaboration), Measurement of event-plane correlations in $\sqrt{s_{NN}} = 2.76$ TeV lead-lead collisions with the ATLAS detector, Phys. Rev. C **90**, 024905 (2014).

[9] B. Alver *et al.* (PHOBOS Collaboration), System Size, Energy, Pseudorapidity, and Centrality Dependence of Elliptic Flow, Phys. Rev. Lett. **98**, 242302 (2007).

[10] B. Alver *et al.* (PHOBOS Collaboration), Event-By-Event Fluctuations of Azimuthal Particle Anisotropy in Au + Au Collisions at $\sqrt{s_{NN}} = 200$ GeV, Phys. Rev. Lett. **104**, 142301 (2010).

[11] G. Aad *et al.* (ATLAS Collaboration), Measurement of the distributions of event-by-event flow harmonics in lead-lead collisions at =2.76 TeV with the ATLAS detector at the LHC, J. High Energy Phys. 11 (2013) 183.

[12] B. Abelev *et al.* (ALICE Collaboration), Anisotropic flow of charged hadrons, pions and (anti-)protons measured at high transverse momentum in Pb-Pb collisions at $\sqrt{s_{NN}} = 2.76$ TeV, Phys. Lett. B **719**, 18 (2013).

[13] K. Aamodt *et al.* (ALICE Collaboration), Higher Harmonic Anisotropic Flow Measurements of Charged Particles in Pb-Pb Collisions at $\sqrt{s_{NN}} = 2.76$ TeV, Phys. Rev. Lett. **107**, 032301 (2011).

[14] S. Chatrchyan *et al.* (CMS Collaboration), Studies of azimuthal dihadron correlations in ultra-central PbPb collisions at $\sqrt{s_{NN}} = 2.76$ TeV, J. High Energy Phys. 02 (2014) 088.

[15] B. B. Abelev *et al.* (ALICE Collaboration), Long-range angular correlations of π, K and p in p-Pb collisions at $\sqrt{s_{NN}} = 5.02$ TeV, Phys. Lett. B **726**, 164 (2013).

[16] B. B. Abelev *et al.* (ALICE Collaboration), Multiplicity dependence of pion, kaon, proton and lambda production in p-Pb collisions at $\sqrt{s_{NN}} = 5.02$ TeV, Phys. Lett. B **728**, 25 (2014).

[17] K. Werner, M. Bleicher, B. Guiot, I. Karpenko, and T. Pierog, Evidence for Flow in *p*-Pb Collisions at 5 TeV from v2 Mass Splitting, Phys. Rev. Lett. **112**, 232301 (2014).

[18] E. Shuryak and I. Zahed, High-multiplicity *pp* and *pA* collisions: Hydrodynamics at its edge, Phys. Rev. C **88**, 044915 (2013).

[19] P. Bozek, W. Broniowski, and G. Torrieri, Hydrodynamic models of particle production - p-Pb collisions, J. Phys. Conf. Ser. **509**, 012017 (2014).

[20] J. Schukraft, A. Timmins, and S. A. Voloshin, Ultra-relativistic nuclear collisions: Event shape engineering, Phys. Lett. B **719**, 394 (2013).

[21] F. G. Gardim, F. Grassi, M. Luzum, and J.-Y. Ollitrault, Characterizing the hydrodynamic response to the initial conditions, Nucl. Phys. A **904**, 503c (2013).

[22] S. A. Voloshin, A. M. Poskanzer, and R. Snellings, *Collective phenomena in non-central nuclear collisions*, in Landolt-Boernstein, Relativistic Heavy Ion Physics, Vol. 1/23 (Springer-Verlag, 2010), pp. 5–54.

[23] G. Aad *et al.* (ATLAS Collaboration), Measurement of the correlation between flow harmonics of different order in lead-lead collisions at $\sqrt{s_{NN}} = 2.76$ TeV with the ATLAS detector, Phys. Rev. C **92**, 034903 (2015).

[24] K. Aamodt *et al.* (ALICE Collaboration), The ALICE experiment at the CERN LHC, JINST **3**, S08002 (2008).

[25] J. Alme, Y. Andres, H. Appelshauser, S. Bablok, N. Bialas *et al.*, The ALICE TPC, a large 3-dimensional tracking device with fast readout for ultra-high multiplicity events, Nucl. Instrum. Methods A **622**, 316 (2010).

[26] B. B. Abelev *et al.* (ALICE Collaboration), Performance of the ALICE Experiment at the CERN LHC, Int. J. Mod. Phys. A **29**, 1430044 (2014).

[27] ALICE Collaboration, Technical design report of the time projection chamber, Technical Report CERN/LHCC 2000-001, 2000.

[28] E. Abbas *et al.* (ALICE Collaboration), Performance of the ALICE VZERO system, J. Instrum. **8**, P10016 (2013).

[29] B. Abelev *et al.* (ALICE Collaboration), Centrality determination of Pb-Pb collisions at $\sqrt{s_{NN}} = 2.76$ TeV with ALICE, Phys. Rev. C **88**, 044909 (2013).

[30] K. Aamodt *et al.* (ALICE Collaboration), Charged-Particle Multiplicity Density at Mid-Rapidity in Central Pb-Pb Collisions at $\sqrt{s_{NN}} = 2.76$ TeV, Phys. Rev. Lett. **105**, 252301 (2010).

[31] K. Aamodt *et al.* (ALICE Collaboration), Centrality Dependence of the Charged-Particle Multiplicity Density at Mid-Rapidity in Pb-Pb Collisions at $\sqrt{s_{NN}} = 2.76$ TeV, Phys. Rev. Lett. **106**, 032301 (2011).

[32] C. Adler *et al.* (STAR Collaboration), Elliptic flow from two and four particle correlations in Au+Au collisions at s(NN)**(1/2) = 130-GeV, Phys. Rev. C **66**, 034904 (2002).

[33] Z.-W. Lin, C. M. Ko, B.-A. Li, B. Zhang, and S. Pal, A Multi-phase transport model for relativistic heavy ion collisions, Phys. Rev. C **72**, 064901 (2005).

[34] R. Brun, F. Carminati, and S. Giani, GEANT detector description and simulation tool, CERN-W5013.

[35] B. Abelev *et al.* (ALICE Collaboration), Measurement of charged jet suppression in Pb-Pb collisions at $\sqrt{s_{NN}} = 2.76$ TeV, J. High Energy Phys. 03 (2014) 013.

[36] R. Barlow, Systematic errors: Facts and fictions, arXiv:hep-ex/0207026 [hep-ex].

[37] B. Abelev *et al.* (ALICE Collaboration), Centrality dependence of charged particle production at large transverse momentum in Pb-Pb collisions at $\sqrt{s_{NN}} = 2.76$ TeV, Phys. Lett. B **720**, 52 (2013).

[38] B. Abelev *et al.* (ALICE Collaboration), Centrality dependence of π, K, p production in Pb-Pb collisions at $\sqrt{s_{NN}} = 2.76$ TeV, Phys. Rev. C **88**, 044910 (2013).

[39] B. B. Abelev *et al.* (ALICE Collaboration), Elliptic flow of identified hadrons in Pb-Pb collisions at $\sqrt{s_{NN}} = 2.76$ TeV, J. High Energy Phys. 06 (2015) 190.

[40] E. Schnedermann, J. Sollfrank, and U. W. Heinz, Thermal phenomenology of hadrons from 200-A/GeV S+S collisions, Phys. Rev. C **48**, 2462 (1993).

[41] S. Voloshin and A. M. Poskanzer, The physics of the centrality dependence of elliptic flow, Phys. Lett. B **474**, 27 (2000).

[42] B. Alver, B. Back, M. Baker, M. Ballintijn, D. Barton *et al.*, Importance of correlations and fluctuations on the initial source eccentricity in high-energy nucleus-nucleus collisions, Phys. Rev. C **77**, 014906 (2008).

[43] S. A. Voloshin, A. M. Poskanzer, A. Tang, and G. Wang, Elliptic flow in the Gaussian model of eccentricity fluctuations, Phys. Lett. B **659**, 537 (2008).

[44] H. Song and U. W. Heinz, Interplay of shear and bulk viscosity in generating flow in heavy-ion collisions, Phys. Rev. C **81**, 024905 (2010).

[45] P. Bozek and W. Broniowski, Transverse-momentum fluctuations in relativistic heavy-ion collisions from event-by-event viscous hydrodynamics, Phys. Rev. C **85**, 044910 (2012).

[46] W. Broniowski, M. Chojnacki, and L. Obara, Size fluctuations of the initial source and the event-by-event transverse momentum fluctuations in relativistic heavy-ion collisions, Phys. Rev. C **80**, 051902 (2009).

[47] R. S. Bhalerao, J.-Y. Ollitrault, S. Pal, and D. Teaney, Principal Component Analysis of Event-By-Event Fluctuations, Phys. Rev. Lett. **114**, 152301 (2015).

[48] A. Mazeliauskas and D. Teaney, Subleading harmonic flows in hydrodynamic simulations of heavy ion collisions, Phys. Rev. C **91**, 044902 (2015).

[49] A. Mazeliauskas and D. Teaney, Fluctuations of harmonic and radial flow in heavy ion collisions with principal components, Phys. Rev. C **93**, 024913 (2016).

[50] M. Gyulassy and X.-N. Wang, HIJING1.0: A Monte Carlo program for parton and particle production in high-energy hadronic and nuclear collisions, Comput. Phys. Commun. **83**, 307 (1994).

[51] B. Zhang, ZPC 1.0.1: A Parton cascade for ultrarelativistic heavy ion collisions, Comput. Phys. Commun. **109**, 193 (1998).

[52] B. Abelev *et al.* (ALICE Collaboration), Charge correlations using the balance function in Pb-Pb collisions at $\sqrt{s_{NN}} = 2.76$ TeV, Phys. Lett. B **723**, 267 (2013).

J. Adam,[40] D. Adamová,[83] M. M. Aggarwal,[87] G. Aglieri Rinella,[36] M. Agnello,[111] N. Agrawal,[48] Z. Ahammed,[132] S. U. Ahn,[68] I. Aimo,[94,111] S. Aiola,[136] M. Ajaz,[16] A. Akindinov,[58] S. N. Alam,[132] D. Aleksandrov,[100] B. Alessandro,[111] D. Alexandre,[102] R. Alfaro Molina,[64] A. Alici,[105,12] J. R. M. Almaraz,[119] J. Alme,[38] T. Alt,[43] S. Altinpinar,[18] I. Altsybeev,[131] C. Alves Garcia Prado,[120] C. Andrei,[78] A. Andronic,[97] V. Anguelov,[93] J. Anielski,[54] T. Antičić,[98] F. Antinori,[108] P. Antonioli,[105] L. Aphecetche,[113] H. Appelshäuser,[53] S. Arcelli,[28] N. Armesto,[17] R. Arnaldi,[111] I. C. Arsene,[22] M. Arslandok,[53]

B. Audurier,[113] A. Augustinus,[36] R. Averbeck,[97] M. D. Azmi,[19] M. Bach,[43] A. Badalà,[107] Y. W. Baek,[44] S. Bagnasco,[111] R. Bailhache,[53] R. Bala,[90] A. Baldisseri,[15] F. Baltasar Dos Santos Pedrosa,[36] R. C. Baral,[61] A. M. Barbano,[111] R. Barbera,[29] F. Barile,[33] G. G. Barnaföldi,[135] L. S. Barnby,[102] V. Barret,[70] P. Bartalini,[7] K. Barth,[36] J. Bartke,[117] E. Bartsch,[53] M. Basile,[28] N. Bastid,[70] S. Basu,[132] B. Bathen,[54] G. Batigne,[113] A. Batista Camejo,[70] B. Batyunya,[66] P. C. Batzing,[22] I. G. Bearden,[80] H. Beck,[53] C. Bedda,[111] N. K. Behera,[48,49] I. Belikov,[55] F. Bellini,[28] H. Bello Martinez,[2] R. Bellwied,[122] R. Belmont,[134] E. Belmont-Moreno,[64] V. Belyaev,[76] G. Bencedi,[135] S. Beole,[27] I. Berceanu,[78] A. Bercuci,[78] Y. Berdnikov,[85] D. Berenyi,[135] R. A. Bertens,[57] D. Berzano,[36,27] L. Betev,[36] A. Bhasin,[90] I. R. Bhat,[90] A. K. Bhati,[87] B. Bhattacharjee,[45] J. Bhom,[128] L. Bianchi,[122] N. Bianchi,[72] C. Bianchin,[134,57] J. Bielčík,[40] J. Bielčíková,[83] A. Bilandzic,[80] R. Biswas,[4] S. Biswas,[79] S. Bjelogrlic,[57] J. T. Blair,[118] F. Blanco,[10] D. Blau,[100] C. Blume,[53] F. Bock,[93,74] A. Bogdanov,[76] H. Bøggild,[80] L. Boldizsár,[135] M. Bombara,[41] J. Book,[53] H. Borel,[15] A. Borissov,[96] M. Borri,[82] F. Bossú,[65] E. Botta,[27] S. Böttger,[52] P. Braun-Munzinger,[97] M. Bregant,[120] T. Breitner,[52] T. A. Broker,[53] T. A. Browning,[95] M. Broz,[40] E. J. Brucken,[46] E. Bruna,[111] G. E. Bruno,[33] D. Budnikov,[99] H. Buesching,[53] S. Bufalino,[27,111] P. Buncic,[36] O. Busch,[128,93] Z. Buthelezi,[65] J. B. Butt,[16] J. T. Buxton,[20] D. Caffarri,[36] X. Cai,[7] H. Caines,[136] L. Calero Diaz,[72] A. Caliva,[57] E. Calvo Villar,[103] P. Camerini,[26] F. Carena,[36] W. Carena,[36] F. Carnesecchi,[28] J. Castillo Castellanos,[15] A. J. Castro,[125] E. A. R. Casula,[25] C. Cavicchioli,[36] C. Ceballos Sanchez,[9] J. Cepila,[40] P. Cerello,[111] J. Cerkala,[115] B. Chang,[123] S. Chapeland,[36] M. Chartier,[124] J. L. Charvet,[15] S. Chattopadhyay,[132] S. Chattopadhyay,[101] V. Chelnokov,[3] M. Cherney,[86] C. Cheshkov,[130] B. Cheynis,[130] V. Chibante Barroso,[36] D. D. Chinellato,[121] P. Chochula,[36] K. Choi,[96] M. Chojnacki,[80] S. Choudhury,[132] P. Christakoglou,[81] C. H. Christensen,[80] P. Christiansen,[34] T. Chujo,[128] S. U. Chung,[96] Z. Chunhui,[57] C. Cicalo,[106] L. Cifarelli,[12,28] F. Cindolo,[105] J. Cleymans,[89] F. Colamaria,[33] D. Colella,[36,33,59] A. Collu,[25] M. Colocci,[28] G. Conesa Balbastre,[71] Z. Conesa del Valle,[51] M. E. Connors,[136] J. G. Contreras,[11,40] T. M. Cormier,[84] Y. Corrales Morales,[27] I. Cortés Maldonado,[2] P. Cortese,[32] M. R. Cosentino,[120] F. Costa,[36] P. Crochet,[70] R. Cruz Albino,[11] E. Cuautle,[63] L. Cunqueiro,[36] T. Dahms,[92,37] A. Dainese,[108] A. Danu,[62] D. Das,[101] I. Das,[101,51] S. Das,[4] A. Dash,[121] S. Dash,[48] S. De,[120] A. De Caro,[31,12] G. de Cataldo,[104] J. de Cuveland,[43] A. De Falco,[25] D. De Gruttola,[12,31] N. De Marco,[111] S. De Pasquale,[31] A. Deisting,[97,93] A. Deloff,[77] E. Dénes,[135,*] G. D'Erasmo,[33] D. Di Bari,[33] A. Di Mauro,[36] P. Di Nezza,[72] M. A. Diaz Corchero,[10] T. Dietel,[89] P. Dillenseger,[53] R. Divià,[36] Ø. Djuvsland,[18] A. Dobrin,[57,81] T. Dobrowolski,[77,*] D. Domenicis Gimenez,[120] B. Dönigus,[53] O. Dordic,[22] T. Drozhzhova,[53] A. K. Dubey,[132] A. Dubla,[57] L. Ducroux,[130] P. Dupieux,[70] R. J. Ehlers,[136] D. Elia,[104] H. Engel,[52] B. Erazmus,[36,113] I. Erdemir,[53] F. Erhardt,[129] D. Eschweiler,[43] B. Espagnon,[51] M. Estienne,[113] S. Esumi,[128] J. Eum,[96] D. Evans,[102] S. Evdokimov,[112] G. Eyyubova,[40] L. Fabbietti,[37,92] D. Fabris,[108] J. Faivre,[71] A. Fantoni,[72] M. Fasel,[74] L. Feldkamp,[54] D. Felea,[62] A. Feliciello,[111] G. Feofilov,[131] J. Ferencei,[83] A. Fernández Téllez,[2] E. G. Ferreiro,[17] A. Ferretti,[27] A. Festanti,[30] V. J. G. Feuillard,[15,70] J. Figiel,[117] M. A. S. Figueredo,[124,120] S. Filchagin,[99] D. Finogeev,[56] F. M. Fionda,[25] E. M. Fiore,[33] M. G. Fleck,[93] M. Floris,[36] S. Foertsch,[65] P. Foka,[97] S. Fokin,[100] E. Fragiacomo,[110] A. Francescon,[36,30] U. Frankenfeld,[97] U. Fuchs,[36] C. Furget,[71] A. Furs,[56] M. Fusco Girard,[31] J. J. Gaardhøje,[80] M. Gagliardi,[27] A. M. Gago,[103] M. Gallio,[27] D. R. Gangadharan,[74] P. Ganoti,[88] C. Gao,[7] C. Garabatos,[97] E. Garcia-Solis,[13] C. Gargiulo,[36] P. Gasik,[92,37] M. Germain,[113] A. Gheata,[36] M. Gheata,[62,36] P. Ghosh,[132] S. K. Ghosh,[4] P. Gianotti,[72] P. Giubellino,[36] P. Giubilato,[30] E. Gladysz-Dziadus,[117] P. Glässel,[93] D. M. Goméz Coral,[64] A. Gomez Ramirez,[52] P. González-Zamora,[10] S. Gorbunov,[43] L. Görlich,[117] S. Gotovac,[116] V. Grabski,[64] L. K. Graczykowski,[133] K. L. Graham,[102] A. Grelli,[57] A. Grigoras,[36] C. Grigoras,[36] V. Grigoriev,[76] A. Grigoryan,[1] S. Grigoryan,[66] B. Grinyov,[3] N. Grion,[110] J. F. Grosse-Oetringhaus,[36] J.-Y. Grossiord,[130] R. Grosso,[36] F. Guber,[56] R. Guernane,[71] B. Guerzoni,[28] K. Gulbrandsen,[80] H. Gulkanyan,[1] T. Gunji,[127] A. Gupta,[90] R. Gupta,[90] R. Haake,[54] Ø. Haaland,[18] C. Hadjidakis,[51] M. Haiduc,[62] H. Hamagaki,[127] G. Hamar,[135] A. Hansen,[80] J. W. Harris,[136] H. Hartmann,[43] A. Harton,[13] D. Hatzifotiadou,[105] S. Hayashi,[127] S. T. Heckel,[53] M. Heide,[54] H. Helstrup,[38] A. Herghelegiu,[78] G. Herrera Corral,[11] B. A. Hess,[35] K. F. Hetland,[38] T. E. Hilden,[46] H. Hillemanns,[36] B. Hippolyte,[55] R. Hosokawa,[128] P. Hristov,[36] M. Huang,[18] T. J. Humanic,[20] N. Hussain,[45] T. Hussain,[19] D. Hutter,[43] D. S. Hwang,[21] R. Ilkaev,[99] I. Ilkiv,[77] M. Inaba,[128] M. Ippolitov,[76,100] M. Irfan,[19] M. Ivanov,[97] V. Ivanov,[85] V. Izucheev,[112] P. M. Jacobs,[74] S. Jadlovska,[115] C. Jahnke,[120] H. J. Jang,[68] M. A. Janik,[133] P. H. S. Y. Jayarathna,[122] C. Jena,[30] S. Jena,[122] R. T. Jimenez Bustamante,[97] P. G. Jones,[102] H. Jung,[44] A. Jusko,[102] P. Kalinak,[59] A. Kalweit,[36] J. Kamin,[53] J. H. Kang,[137] V. Kaplin,[76] S. Kar,[132] A. Karasu Uysal,[69] O. Karavichev,[56] T. Karavicheva,[56] L. Karayan,[93,97] E. Karpechev,[56] U. Kebschull,[52] R. Keidel,[138] D. L. D. Keijdener,[57] M. Keil,[36] K. H. Khan,[16] M. Mohisin Khan,[19] P. Khan,[101] S. A. Khan,[132] A. Khanzadeev,[85] Y. Kharlov,[112] B. Kileng,[38] B. Kim,[137] D. W. Kim,[44,68] D. J. Kim,[123] H. Kim,[137] J. S. Kim,[44] M. Kim,[44] M. Kim,[137] S. Kim,[21] T. Kim,[137] S. Kirsch,[43] I. Kisel,[43] S. Kiselev,[58] A. Kisiel,[133] G. Kiss,[135] J. L. Klay,[6] C. Klein,[53] J. Klein,[36,93] C. Klein-Bösing,[54] A. Kluge,[36] M. L. Knichel,[93] A. G. Knospe,[118] T. Kobayashi,[128] C. Kobdaj,[114] M. Kofarago,[36] T. Kollegger,[97,43] A. Kolojvari,[131] V. Kondratiev,[131] N. Kondratyeva,[76] E. Kondratyuk,[112] A. Konevskikh,[56] M. Kopcik,[115] M. Kour,[90] C. Kouzinopoulos,[36] O. Kovalenko,[77] V. Kovalenko,[131] M. Kowalski,[117] G. Koyithatta Meethaleveedu,[48] J. Kral,[123] I. Králik,[59] A. Kravčáková,[41] M. Kretz,[43] M. Krivda,[59,102] F. Krizek,[83] E. Kryshen,[36] M. Krzewicki,[43] A. M. Kubera,[20] V. Kučera,[83] T. Kugathasan,[36] C. Kuhn,[55] P. G. Kuijer,[81] A. Kumar,[90] J. Kumar,[48] L. Kumar,[79,87] P. Kurashvili,[77] A. Kurepin,[56] A. B. Kurepin,[56] A. Kuryakin,[99] S. Kushpil,[83] M. J. Kweon,[50] Y. Kwon,[137] S. L. La Pointe,[111] P. La Rocca,[29] C. Lagana Fernandes,[120] I. Lakomov,[36] R. Langoy,[42] C. Lara,[52] A. Lardeux,[15] A. Lattuca,[27] E. Laudi,[36] R. Lea,[26] L. Leardini,[93] G. R. Lee,[102] S. Lee,[137] I. Legrand,[36] F. Lehas,[81] R. C. Lemmon,[82] V. Lenti,[104] E. Leogrande,[57] I. León Monzón,[119] M. Leoncino,[27] P. Lévai,[135] S. Li,[7,70] X. Li,[14] J. Lien,[42] R. Lietava,[102] S. Lindal,[22] V. Lindenstruth,[43] C. Lippmann,[97]

M. A. Lisa,[20] H. M. Ljunggren,[34] D. F. Lodato,[57] P. I. Loenne,[18] V. Loginov,[76] C. Loizides,[74] X. Lopez,[70] E. López Torres,[9] A. Lowe,[135] P. Luettig,[53] M. Lunardon,[30] G. Luparello,[26] P. H. F. N. D. Luz,[120] A. Maevskaya,[56] M. Mager,[36] S. Mahajan,[90] S. M. Mahmood,[22] A. Maire,[55] R. D. Majka,[136] M. Malaev,[85] I. Maldonado Cervantes,[63] L. Malinina,[66,†] D. Mal'Kevich,[58] P. Malzacher,[97] A. Mamonov,[99] V. Manko,[100] F. Manso,[70] V. Manzari,[36,104] M. Marchisone,[27] J. Mareš,[60] G. V. Margagliotti,[26] A. Margotti,[105] J. Margutti,[57] A. Marín,[97] C. Markert,[118] M. Marquard,[53] N. A. Martin,[97] J. Martin Blanco,[113] P. Martinengo,[36] M. I. Martínez,[2] G. Martínez García,[113] M. Martinez Pedreira,[36] Y. Martynov,[3] A. Mas,[120] S. Masciocchi,[97] M. Masera,[27] A. Masoni,[106] L. Massacrier,[113] A. Mastroserio,[33] H. Masui,[128] A. Matyja,[117] C. Mayer,[117] J. Mazer,[125] M. A. Mazzoni,[109] D. Mcdonald,[122] F. Meddi,[24] Y. Melikyan,[76] A. Menchaca-Rocha,[64] E. Meninno,[31] J. Mercado Pérez,[93] M. Meres,[39] Y. Miake,[128] M. M. Mieskolainen,[46] K. Mikhaylov,[66,58] L. Milano,[36] J. Milosevic,[22] L. M. Minervini,[104,23] A. Mischke,[57] A. N. Mishra,[49] D. Miśkowiec,[97] J. Mitra,[132] C. M. Mitu,[62] N. Mohammadi,[57] B. Mohanty,[132,79] L. Molnar,[55] L. Montaño Zetina,[11] E. Montes,[10] M. Morando,[30] D. A. Moreira De Godoy,[113,54] S. Moretto,[30] A. Morreale,[113] A. Morsch,[36] V. Muccifora,[72] E. Mudnic,[116] D. Mühlheim,[54] S. Muhuri,[132] M. Mukherjee,[132] J. D. Mulligan,[136] M. G. Munhoz,[120] S. Murray,[65] L. Musa,[36] J. Musinsky,[59] B. K. Nandi,[48] R. Nania,[105] E. Nappi,[104] M. U. Naru,[16] C. Nattrass,[125] K. Nayak,[79] T. K. Nayak,[132] S. Nazarenko,[99] A. Nedosekin,[58] L. Nellen,[63] F. Ng,[122] M. Nicassio,[97] M. Niculescu,[62,36] J. Niedziela,[36] B. S. Nielsen,[80] S. Nikolaev,[100] S. Nikulin,[100] V. Nikulin,[85] F. Noferini,[105,12] P. Nomokonov,[66] G. Nooren,[57] J. C. C. Noris,[2] J. Norman,[124] A. Nyanin,[100] J. Nystrand,[18] H. Oeschler,[93] S. Oh,[136] S. K. Oh,[67] A. Ohlson,[36] A. Okatan,[69] T. Okubo,[47] L. Olah,[135] J. Oleniacz,[133] A. C. Oliveira Da Silva,[120] M. H. Oliver,[136] J. Onderwaater,[97] C. Oppedisano,[111] R. Orava,[46] A. Ortiz Velasquez,[63] A. Oskarsson,[34] J. Otwinowski,[117] K. Oyama,[93] M. Ozdemir,[53] Y. Pachmayer,[93] P. Pagano,[31] G. Paić,[63] C. Pajares,[17] S. K. Pal,[132] J. Pan,[134] A. K. Pandey,[48] D. Pant,[48] P. Papcun,[115] V. Papikyan,[1] G. S. Pappalardo,[107] P. Pareek,[49] W. J. Park,[97] S. Parmar,[87] A. Passfeld,[54] V. Paticchio,[104] R. N. Patra,[132] B. Paul,[101] T. Peitzmann,[57] H. Pereira Da Costa,[15] E. Pereira De Oliveira Filho,[120] D. Peresunko,[100,76] C. E. Pérez Lara,[81] E. Perez Lezama,[53] V. Peskov,[53] Y. Pestov,[5] V. Petráček,[40] V. Petrov,[112] M. Petrovici,[78] C. Petta,[29] S. Piano,[110] M. Pikna,[39] P. Pillot,[113] O. Pinazza,[105,36] L. Pinsky,[122] D. B. Piyarathna,[122] M. Płoskoń,[74] M. Planinic,[129] J. Pluta,[133] S. Pochybova,[135] P. L. M. Podesta-Lerma,[119] M. G. Poghosyan,[86,84] B. Polichtchouk,[112] N. Poljak,[129] W. Poonsawat,[114] A. Pop,[78] S. Porteboeuf-Houssais,[70] J. Porter,[74] J. Pospisil,[83] S. K. Prasad,[4] R. Preghenella,[36,105] F. Prino,[111] C. A. Pruneau,[134] I. Pshenichnov,[56] M. Puccio,[111] G. Puddu,[25] P. Pujahari,[134] V. Punin,[99] J. Putschke,[134] H. Qvigstad,[22] A. Rachevski,[110] S. Raha,[4] S. Rajput,[90] J. Rak,[123] A. Rakotozafindrabe,[15] L. Ramello,[32] F. Rami,[55] R. Raniwala,[91] S. Raniwala,[91] S. S. Räsänen,[46] B. T. Rascanu,[53] D. Rathee,[87] K. F. Read,[125] J. S. Real,[71] K. Redlich,[77] R. J. Reed,[134] A. Rehman,[18] P. Reichelt,[53] F. Reidt,[93,36] X. Ren,[7] R. Renfordt,[53] A. R. Reolon,[72] A. Reshetin,[56] F. Rettig,[43] J.-P. Revol,[12] K. Reygers,[93] V. Riabov,[85] R. A. Ricci,[73] T. Richert,[34] M. Richter,[22] P. Riedler,[36] W. Riegler,[36] F. Riggi,[29] C. Ristea,[62] A. Rivetti,[111] E. Rocco,[57] M. Rodríguez Cahuantzi,[2] A. Rodriguez Manso,[81] K. Røed,[22] E. Rogochaya,[66] D. Rohr,[43] D. Röhrich,[18] R. Romita,[124] F. Ronchetti,[72] L. Ronflette,[113] P. Rosnet,[70] A. Rossi,[30,36] F. Roukoutakis,[88] A. Roy,[49] C. Roy,[55] P. Roy,[101] A. J. Rubio Montero,[10] R. Rui,[26] R. Russo,[27] E. Ryabinkin,[100] Y. Ryabov,[85] A. Rybicki,[117] S. Sadovsky,[112] K. Šafařík,[36] B. Sahlmuller,[53] P. Sahoo,[49] R. Sahoo,[49] S. Sahoo,[61] P. K. Sahu,[61] J. Saini,[132] S. Sakai,[72] M. A. Saleh,[134] C. A. Salgado,[17] J. Salzwedel,[20] S. Sambyal,[90] V. Samsonov,[85] X. Sanchez Castro,[55] L. Šándor,[59] A. Sandoval,[64] M. Sano,[128] D. Sarkar,[132] E. Scapparone,[105] F. Scarlassara,[30] R. P. Scharenberg,[95] C. Schiaua,[78] R. Schicker,[93] C. Schmidt,[97] H. R. Schmidt,[35] S. Schuchmann,[53] J. Schukraft,[36] M. Schulc,[40] T. Schuster,[136] Y. Schutz,[113,36] K. Schwarz,[97] K. Schweda,[97] G. Scioli,[28] E. Scomparin,[111] R. Scott,[125] J. E. Seger,[86] Y. Sekiguchi,[127] D. Sekihata,[47] I. Selyuzhenkov,[97] K. Senosi,[65] J. Seo,[96,67] E. Serradilla,[64,10] A. Sevcenco,[62] A. Shabanov,[56] A. Shabetai,[113] O. Shadura,[3] R. Shahoyan,[36] A. Shangaraev,[112] A. Sharma,[90] M. Sharma,[90] M. Sharma,[90] N. Sharma,[125,61] K. Shigaki,[47] K. Shtejer,[9,27] Y. Sibiriak,[100] S. Siddhanta,[106] K. M. Sielewicz,[36] T. Siemiarczuk,[77] D. Silvermyr,[84,34] C. Silvestre,[71] G. Simatovic,[129] G. Simonetti,[36] R. Singaraju,[132] R. Singh,[79] S. Singha,[132,79] V. Singhal,[132] B. C. Sinha,[132] T. Sinha,[101] B. Sitar,[39] M. Sitta,[32] T. B. Skaali,[22] M. Slupecki,[123] N. Smirnov,[136] R. J. M. Snellings,[57] T. W. Snellman,[123] C. Søgaard,[34] R. Soltz,[75] J. Song,[96] M. Song,[137] Z. Song,[7] F. Soramel,[30] S. Sorensen,[125] M. Spacek,[40] E. Spiriti,[72] I. Sputowska,[117] M. Spyropoulou-Stassinaki,[88] B. K. Srivastava,[95] J. Stachel,[93] I. Stan,[62] G. Stefanek,[77] M. Steinpreis,[20] E. Stenlund,[34] G. Steyn,[65] J. H. Stiller,[93] D. Stocco,[113] P. Strmen,[39] A. A. P. Suaide,[120] T. Sugitate,[47] C. Suire,[51] M. Suleymanov,[16] R. Sultanov,[58] M. Šumbera,[83] T. J. M. Symons,[74] A. Szabo,[39] A. Szanto de Toledo,[120,*] I. Szarka,[39] A. Szczepankiewicz,[36] M. Szymanski,[133] U. Tabassam,[16] J. Takahashi,[121] G. J. Tambave,[18] N. Tanaka,[128] M. A. Tangaro,[33] J. D. Tapia Takaki,[51,‡] A. Tarantola Peloni,[53] M. Tarhini,[51] M. Tariq,[19] M. G. Tarzila,[78] A. Tauro,[36] G. Tejeda Muñoz,[2] A. Telesca,[36] K. Terasaki,[127] C. Terrevoli,[30,25] B. Teyssier,[130] J. Thäder,[74,97] D. Thomas,[118] R. Tieulent,[130] A. R. Timmins,[122] A. Toia,[53] S. Trogolo,[111] V. Trubnikov,[3] W. H. Trzaska,[123] T. Tsuji,[127] A. Tumkin,[99] R. Turrisi,[108] T. S. Tveter,[22] K. Ullaland,[18] A. Uras,[130] G. L. Usai,[25] A. Utrobicic,[129] M. Vajzer,[83] M. Vala,[59] L. Valencia Palomo,[70] S. Vallero,[27] J. Van Der Maarel,[57] J. W. Van Hoorne,[36] M. van Leeuwen,[57] T. Vanat,[83] P. Vande Vyvre,[36] D. Varga,[135] A. Vargas,[2] M. Vargyas,[123] R. Varma,[48] M. Vasileiou,[88] A. Vasiliev,[100] A. Vauthier,[71] V. Vechernin,[131] A. M. Veen,[57] M. Veldhoen,[57] A. Velure,[18] M. Venaruzzo,[73] E. Vercellin,[27] S. Vergara Limón,[2] R. Vernet,[8] M. Verweij,[134,36] L. Vickovic,[116] G. Viesti,[30,*] J. Viinikainen,[123] Z. Vilakazi,[126] O. Villalobos Baillie,[102] A. Vinogradov,[100] L. Vinogradov,[131] Y. Vinogradov,[99,*] T. Virgili,[31] V. Vislavicius,[34] Y. P. Viyogi,[132] A. Vodopyanov,[66] M. A. Völkl,[93] K. Voloshin,[58] S. A. Voloshin,[134] G. Volpe,[135,36] B. von Haller,[36] I. Vorobyev,[37,92] D. Vranic,[36,97] J. Vrláková,[41] B. Vulpescu,[70] A. Vyushin,[99] B. Wagner,[18] J. Wagner,[97] H. Wang,[57] M. Wang,[7,113] Y. Wang,[93] D. Watanabe,[128] Y. Watanabe,[127] M. Weber,[36] S. G. Weber,[97] J. P. Wessels,[54] U. Westerhoff,[54] J. Wiechula,[35] J. Wikne,[22] M. Wilde,[54] G. Wilk,[77] J. Wilkinson,[93] M. C. S. Williams,[105]

B. Windelband,[93] M. Winn,[93] C. G. Yaldo,[134] H. Yang,[57] P. Yang,[7] S. Yano,[47] Z. Yin,[7] H. Yokoyama,[128] I.-K. Yoo,[96]
V. Yurchenko,[3] I. Yushmanov,[100] A. Zaborowska,[133] V. Zaccolo,[80] A. Zaman,[16] C. Zampolli,[105] H. J. C. Zanoli,[120]
S. Zaporozhets,[66] N. Zardoshti,[102] A. Zarochentsev,[131] P. Závada,[60] N. Zaviyalov,[99] H. Zbroszczyk,[133] I. S. Zgura,[62]
M. Zhalov,[85] H. Zhang,[18,7] X. Zhang,[74] Y. Zhang,[7] C. Zhao,[22] N. Zhigareva,[58] D. Zhou,[7] Y. Zhou,[80,57] Z. Zhou,[18] H. Zhu,[18,7]
J. Zhu,[7,113] X. Zhu,[7] A. Zichichi,[28,12] A. Zimmermann,[93] M. B. Zimmermann,[36,54] G. Zinovjev,[3] and M. Zyzak[43]

(ALICE Collaboration)

[1]*A. I. Alikhanyan National Science Laboratory (Yerevan Physics Institute) Foundation, Yerevan, Armenia*
[2]*Benemérita Universidad Autónoma de Puebla, Puebla, Mexico*
[3]*Bogolyubov Institute for Theoretical Physics, Kiev, Ukraine*
[4]*Bose Institute, Department of Physics and Centre for Astroparticle Physics and Space Science (CAPSS), Kolkata, India*
[5]*Budker Institute for Nuclear Physics, Novosibirsk, Russia*
[6]*California Polytechnic State University, San Luis Obispo, California, USA*
[7]*Central China Normal University, Wuhan, China*
[8]*Centre de Calcul de l'IN2P3, Villeurbanne, France*
[9]*Centro de Aplicaciones Tecnológicas y Desarrollo Nuclear (CEADEN), Havana, Cuba*
[10]*Centro de Investigaciones Energéticas Medioambientales y Tecnológicas (CIEMAT), Madrid, Spain*
[11]*Centro de Investigación y de Estudios Avanzados (CINVESTAV), Mexico City and Mérida, Mexico*
[12]*Centro Fermi - Museo Storico della Fisica e Centro Studi e Ricerche "Enrico Fermi", Rome, Italy*
[13]*Chicago State University, Chicago, Illinois, USA*
[14]*China Institute of Atomic Energy, Beijing, China*
[15]*Commissariat à l'Energie Atomique, IRFU, Saclay, France*
[16]*COMSATS Institute of Information Technology (CIIT), Islamabad, Pakistan*
[17]*Departamento de Física de Partículas and IGFAE, Universidad de Santiago de Compostela, Santiago de Compostela, Spain*
[18]*Department of Physics and Technology, University of Bergen, Bergen, Norway*
[19]*Department of Physics, Aligarh Muslim University, Aligarh, India*
[20]*Department of Physics, Ohio State University, Columbus, Ohio, USA*
[21]*Department of Physics, Sejong University, Seoul, South Korea*
[22]*Department of Physics, University of Oslo, Oslo, Norway*
[23]*Dipartimento di Elettrotecnica ed Elettronica del Politecnico, Bari, Italy*
[24]*Dipartimento di Fisica dell'Università 'La Sapienza' and Sezione INFN Rome, Italy*
[25]*Dipartimento di Fisica dell'Università and Sezione INFN, Cagliari, Italy*
[26]*Dipartimento di Fisica dell'Università and Sezione INFN, Trieste, Italy*
[27]*Dipartimento di Fisica dell'Università and Sezione INFN, Turin, Italy*
[28]*Dipartimento di Fisica e Astronomia dell'Università and Sezione INFN, Bologna, Italy*
[29]*Dipartimento di Fisica e Astronomia dell'Università and Sezione INFN, Catania, Italy*
[30]*Dipartimento di Fisica e Astronomia dell'Università and Sezione INFN, Padova, Italy*
[31]*Dipartimento di Fisica 'E. R. Caianiello' dell'Università and Gruppo Collegato INFN, Salerno, Italy*
[32]*Dipartimento di Scienze e Innovazione Tecnologica dell'Università del Piemonte Orientale and Gruppo Collegato INFN, Alessandria, Italy*
[33]*Dipartimento Interateneo di Fisica 'M. Merlin' and Sezione INFN, Bari, Italy*
[34]*Division of Experimental High Energy Physics, University of Lund, Lund, Sweden*
[35]*Eberhard Karls Universität Tübingen, Tübingen, Germany*
[36]*European Organization for Nuclear Research (CERN), Geneva, Switzerland*
[37]*Excellence Cluster Universe, Technische Universität München, Munich, Germany*
[38]*Faculty of Engineering, Bergen University College, Bergen, Norway*
[39]*Faculty of Mathematics, Physics and Informatics, Comenius University, Bratislava, Slovakia*
[40]*Faculty of Nuclear Sciences and Physical Engineering, Czech Technical University in Prague, Prague, Czech Republic*
[41]*Faculty of Science, P. J. Šafárik University, Košice, Slovakia*
[42]*Faculty of Technology, Buskerud and Vestfold University College, Vestfold, Norway*
[43]*Frankfurt Institute for Advanced Studies, Johann Wolfgang Goethe-Universität Frankfurt, Frankfurt, Germany*
[44]*Gangneung-Wonju National University, Gangneung, South Korea*
[45]*Gauhati University, Department of Physics, Guwahati, India*
[46]*Helsinki Institute of Physics (HIP), Helsinki, Finland*
[47]*Hiroshima University, Hiroshima, Japan*
[48]*Indian Institute of Technology Bombay (IIT), Mumbai, India*
[49]*Indian Institute of Technology Indore, Indore (IITI), India*
[50]*Inha University, Incheon, South Korea*

[51]*Institut de Physique Nucléaire d'Orsay (IPNO), Université Paris-Sud, CNRS-IN2P3, Orsay, France*

[52]*Institut für Informatik, Johann Wolfgang Goethe-Universität Frankfurt, Frankfurt, Germany*

[53]*Institut für Kernphysik, Johann Wolfgang Goethe-Universität Frankfurt, Frankfurt, Germany*

[54]*Institut für Kernphysik, Westfälische Wilhelms-Universität Münster, Münster, Germany*

[55]*Institut Pluridisciplinaire Hubert Curien (IPHC), Université de Strasbourg, CNRS-IN2P3, Strasbourg, France*

[56]*Institute for Nuclear Research, Academy of Sciences, Moscow, Russia*

[57]*Institute for Subatomic Physics of Utrecht University, Utrecht, Netherlands*

[58]*Institute for Theoretical and Experimental Physics, Moscow, Russia*

[59]*Institute of Experimental Physics, Slovak Academy of Sciences, Košice, Slovakia*

[60]*Institute of Physics, Academy of Sciences of the Czech Republic, Prague, Czech Republic*

[61]*Institute of Physics, Bhubaneswar, India*

[62]*Institute of Space Science (ISS), Bucharest, Romania*

[63]*Instituto de Ciencias Nucleares, Universidad Nacional Autónoma de México, Mexico City, Mexico*

[64]*Instituto de Física, Universidad Nacional Autónoma de México, Mexico City, Mexico*

[65]*iThemba LABS, National Research Foundation, Somerset West, South Africa*

[66]*Joint Institute for Nuclear Research (JINR), Dubna, Russia*

[67]*Konkuk University, Seoul, South Korea*

[68]*Korea Institute of Science and Technology Information, Daejeon, South Korea*

[69]*KTO Karatay University, Konya, Turkey*

[70]*Laboratoire de Physique Corpusculaire (LPC), Clermont Université, Université Blaise Pascal, CNRS–IN2P3, Clermont-Ferrand, France*

[71]*Laboratoire de Physique Subatomique et de Cosmologie, Université Grenoble-Alpes, CNRS-IN2P3, Grenoble, France*

[72]*Laboratori Nazionali di Frascati, INFN, Frascati, Italy*

[73]*Laboratori Nazionali di Legnaro, INFN, Legnaro, Italy*

[74]*Lawrence Berkeley National Laboratory, Berkeley, California, USA*

[75]*Lawrence Livermore National Laboratory, Livermore, California, USA*

[76]*Moscow Engineering Physics Institute, Moscow, Russia*

[77]*National Centre for Nuclear Studies, Warsaw, Poland*

[78]*National Institute for Physics and Nuclear Engineering, Bucharest, Romania*

[79]*National Institute of Science Education and Research, Bhubaneswar, India*

[80]*Niels Bohr Institute, University of Copenhagen, Copenhagen, Denmark*

[81]*Nikhef, Nationaal Instituut voor Subatomaire Fysica, Amsterdam, Netherlands*

[82]*Nuclear Physics Group, STFC Daresbury Laboratory, Daresbury, United Kingdom*

[83]*Nuclear Physics Institute, Academy of Sciences of the Czech Republic, Řež u Prahy, Czech Republic*

[84]*Oak Ridge National Laboratory, Oak Ridge, Tennessee, USA*

[85]*Petersburg Nuclear Physics Institute, Gatchina, Russia*

[86]*Physics Department, Creighton University, Omaha, Nebraska, USA*

[87]*Physics Department, Panjab University, Chandigarh, India*

[88]*Physics Department, University of Athens, Athens, Greece*

[89]*Physics Department, University of Cape Town, Cape Town, South Africa*

[90]*Physics Department, University of Jammu, Jammu, India*

[91]*Physics Department, University of Rajasthan, Jaipur, India*

[92]*Physik Department, Technische Universität München, Munich, Germany*

[93]*Physikalisches Institut, Ruprecht-Karls-Universität Heidelberg, Heidelberg, Germany*

[94]*Politecnico di Torino, Turin, Italy*

[95]*Purdue University, West Lafayette, Indiana, USA*

[96]*Pusan National University, Pusan, South Korea*

[97]*Research Division and ExtreMe Matter Institute EMMI, GSI Helmholtzzentrum für Schwerionenforschung, Darmstadt, Germany*

[98]*Rudjer Bošković Institute, Zagreb, Croatia*

[99]*Russian Federal Nuclear Center (VNIIEF), Sarov, Russia*

[100]*Russian Research Centre Kurchatov Institute, Moscow, Russia*

[101]*Saha Institute of Nuclear Physics, Kolkata, India*

[102]*School of Physics and Astronomy, University of Birmingham, Birmingham, United Kingdom*

[103]*Sección Física, Departamento de Ciencias, Pontificia Universidad Católica del Perú, Lima, Peru*

[104]*Sezione INFN, Bari, Italy*

[105]*Sezione INFN, Bologna, Italy*

[106]*Sezione INFN, Cagliari, Italy*

[107]*Sezione INFN, Catania, Italy*

[108]*Sezione INFN, Padova, Italy*

[109]*Sezione INFN, Rome, Italy*

[110]*Sezione INFN, Trieste, Italy*

[111]*Sezione INFN, Turin, Italy*

[112]*SSC IHEP of NRC Kurchatov institute, Protvino, Russia*

[113]*SUBATECH, Ecole des Mines de Nantes, Université de Nantes, CNRS-IN2P3, Nantes, France*

[114]*Suranaree University of Technology, Nakhon Ratchasima, Thailand*

[115]*Technical University of Košice, Košice, Slovakia*

[116]*Technical University of Split FESB, Split, Croatia*

[117]*The Henryk Niewodniczanski Institute of Nuclear Physics, Polish Academy of Sciences, Cracow, Poland*

[118]*The University of Texas at Austin, Physics Department, Austin, Texas, USA*

[119]*Universidad Autónoma de Sinaloa, Culiacán, Mexico*

[120]*Universidade de São Paulo (USP), São Paulo, Brazil*

[121]*Universidade Estadual de Campinas (UNICAMP), Campinas, Brazil*

[122]*University of Houston, Houston, Texas, USA*

[123]*University of Jyväskylä, Jyväskylä, Finland*

[124]*University of Liverpool, Liverpool, United Kingdom*

[125]*University of Tennessee, Knoxville, Tennessee, USA*

[126]*University of the Witwatersrand, Johannesburg, South Africa*

[127]*University of Tokyo, Tokyo, Japan*

[128]*University of Tsukuba, Tsukuba, Japan*

[129]*University of Zagreb, Zagreb, Croatia*

[130]*Université de Lyon, Université Lyon 1, CNRS/IN2P3, IPN-Lyon, Villeurbanne, France*

[131]*V. Fock Institute for Physics, St. Petersburg State University, St. Petersburg, Russia*

[132]*Variable Energy Cyclotron Centre, Kolkata, India*

[133]*Warsaw University of Technology, Warsaw, Poland*

[134]*Wayne State University, Detroit, Michigan, USA*

[135]*Wigner Research Centre for Physics, Hungarian Academy of Sciences, Budapest, Hungary*

[136]*Yale University, New Haven, Connecticut, USA*

[137]*Yonsei University, Seoul, South Korea*

[138]*Zentrum für Technologietransfer und Telekommunikation (ZTT), Fachhochschule Worms, Worms, Germany*

[*]Deceased.

[†]Also at M.V. Lomonosov Moscow State University, D.V. Skobeltsyn Institute of Nuclear, Physics, Moscow, Russia.

[‡]Also at University of Kansas, Lawrence, Kansas, USA.